

SPECTROSCOPIC ANALYSIS OF PICTOR II: A VERY LOW METALLICITY ULTRA-FAINT DWARF GALAXY BOUND TO THE LARGE MAGELLANIC CLOUD*

A. B. PACE ^{1,†,‡}, T. S. LI ^{2,3}, A. P. JI ^{4,5,6}, J. D. SIMON ⁷, W. CERNY ⁸, A. M. SENKEVICH ⁹,
 A. DRILICA-WAGNER ^{10,5,4,6}, K. BECHTOL ¹¹, C. Y. TAN ^{5,12}, A. CHITI ^{4,5}, D. ERKAL ⁹,
 C. E. MARTÍNEZ-VÁZQUEZ ¹³, P. S. FERGUSON ¹⁴, R. G. KRON ⁴, K. R. ATZBERGER ¹, A. CHATURVEDI ⁹,
 J. A. FRIEMAN ^{4,5,15}, N. KALLIVAYALIL ¹, G. LIMBERG ⁵, G. E. MEDINA ^{2,3}, V. M. PLACCO ¹⁶, A. H. RILEY ¹⁷,
 D. J. SAND ¹⁸, G. S. STRINGFELLOW ¹⁹, R. P. VAN DER MAREL ^{20,21}, J. A. CARBALLO-BELLO ²², Y. CHOI ¹⁶,
 D. CRNOJEVIĆ ²³, P. MASSANA ²⁴, B. MUTLU-PAKDIL ²⁵, M. NAVABI ⁹, N. E. D. NOËL ⁹, AND
 J. D. SAKOWSKA ²⁶

¹ Department of Astronomy, University of Virginia, 530 McCormick Road, Charlottesville, VA 22904, USA

² David A. Dunlap Department of Astronomy & Astrophysics, University of Toronto, 50 St George Street, Toronto ON M5S 3H4, CA
³ Dunlap Institute for Astronomy & Astrophysics, University of Toronto, 50 St George Street, Toronto, ON M5S 3H4, CA

⁴ Department of Astronomy & Astrophysics, University of Chicago, Chicago, IL 60637, USA

⁵ Kavli Institute for Cosmological Physics, University of Chicago, Chicago, IL 60637, USA

⁶ NSF-Simons AI Institute for the Sky (SkAI), 172 E. Chestnut St., Chicago, IL 60611, USA

⁷ Observatories of the Carnegie Institution for Science, 813 Santa Barbara St., Pasadena, CA 91101, USA

⁸ Department of Astronomy, Yale University, New Haven, CT 06520, USA

⁹ School of Mathematics and Physics, University of Surrey, Guildford, Surrey, GU2 7XH, UK

¹⁰ Fermi National Accelerator Laboratory, P.O. Box 500, Batavia, IL 60510, USA

¹¹ Physics Department, 2320 Chamberlin Hall, University of Wisconsin-Madison, 1150 University Avenue Madison, WI 53706-1390

¹² Department of Physics, University of Chicago, Chicago, IL 60637, USA

¹³ NSF NOIRLab, 670 N. A'ohoku Place, Hilo, Hawai'i, 96720, USA

¹⁴ DiRAC Institute, Department of Astronomy, University of Washington, 3910 15th Ave NE, Seattle, WA, 98195, USA

¹⁵ SLAC National Laboratory, 2575 Sand Hill Rd, Menlo Park, CA 94025

¹⁶ NSF NOIRLab, 950 N. Cherry Ave., Tucson, AZ 85719, USA

¹⁷ Institute for Computational Cosmology, Department of Physics, Durham University, South Road, Durham DH1 3LE, UK

¹⁸ Steward Observatory, University of Arizona, 933 North Cherry Avenue, Tucson, AZ 85721-0065, USA

¹⁹ Center for Astrophysics and Space Astronomy, University of Colorado Boulder, Boulder, CO 80309, USA

²⁰ Space Telescope Science Institute, 3700 San Martin Drive, Baltimore, MD 21218, USA

²¹ Center for Astrophysical Sciences, The William H. Miller III Department of Physics & Astronomy, Johns Hopkins University, Baltimore, MD 21218, USA

²² Instituto de Alta Investigación, Universidad de Tarapacá, Casilla 7D, Arica, Chile

²³ Department of Physics and Astronomy, University of Tampa, 401 West Kennedy Boulevard, Tampa, FL 33606, USA

²⁴ NSF NOIRLab, Casilla 603, La Serena, Chile

²⁵ Department of Physics and Astronomy, Dartmouth College, Hanover, NH 03755, USA and

²⁶ Instituto de Astrofísica de Andalucía, CSIC, Glorieta de la Astronomía, E-18080 Granada, Spain

(DELVE & MAGIC COLLABORATIONS)

Version June 30, 2025

Abstract

We present Magellan/IMACS and Magellan/MIKE spectroscopy of the ultra-faint dwarf (UFD) galaxy Pictor II (Pic II) that is located only 12 kpc from the Large Magellanic Cloud (LMC). From the IMACS spectroscopy, we identify 13 member stars and measure a mean heliocentric velocity of $326.9 \pm 1.1 \text{ km s}^{-1}$, a velocity dispersion of $3.5_{-0.9}^{+1.1} \text{ km s}^{-1}$, a mean metallicity of $[\text{Fe}/\text{H}] = -2.99 \pm 0.06$, and an upper limit on the metallicity dispersion of $\sigma_{[\text{Fe}/\text{H}]} < 0.18$. We measure detailed elemental abundances for the brightest star, finding $[\text{Fe}/\text{H}] = -3.3$, high $[\alpha/\text{Fe}]$ ratios, and no detectable neutron capture elements, similar to stars in other UFDs. However, this star has an unusually high $[\text{Sc}/\text{Fe}]$ ratio. The dynamical mass-to-light ratio ($M/L = 760_{-420}^{+910} M_\odot L_\odot^{-1}$), size, and chemical abundances confirms that Pic II is a dark matter-dominated dwarf galaxy. We perform detailed orbit modeling of Pic II in a combined Milky Way (MW) and LMC potential and find that Pic II is highly likely to be a long-term LMC satellite. Furthermore, we find that Pic II is likely still bound to the LMC today. Pic II is the seventh LMC-associated UFD and among the most metal-poor UFDs known. We further update the morphological parameters with deeper Dark Energy Camera (DECam) photometry, compute the dark matter properties for dark matter indirect detection searches, verify the extremely low metallicity with narrowband CaHK imaging, and briefly discuss tidal influences of the LMC and MW.

Subject headings: Dwarf galaxies (416), Stellar abundances (1577), Local Group (929), Spectroscopy (1558)

1. INTRODUCTION

The advent of wide and deep optical surveys has precipitated the discovery of a large number of ultra-faint

dwarf galaxies (UFDs, $M_V \gtrsim -7.7$) around the Milky Way (MW) (e.g., Willman et al. 2005; Belokurov et al. 2007; Laevens et al. 2015; Bechtol et al. 2015; Koposov et al. 2015a; Drlica-Wagner et al. 2015; Cerny et al. 2023b; Smith et al. 2023; Homma et al. 2024; Tan et al. 2025). UFDs are among the oldest, most chemically pristine, and dark matter dominated galaxies known (McConnachie 2012; Simon 2019; Pace 2024) and are excellent probes to test Λ CDM at small scales (Bullock & Boylan-Kolchin 2017). UFDs are old and metal-poor, and their stars trace chemical enrichment from the first Population III stars (Simon & Geha 2007; Brown et al. 2014; Frebel & Norris 2015). The population of UFDs probes galaxy formation before the epoch of reionization (e.g., Bose et al. 2018) and constrains the small-scale power spectrum of dark matter (e.g., Jethwa et al. 2018; Newton et al. 2018; Nadler et al. 2021).

The MW’s most massive companion galaxies, the Large and Small Magellanic Clouds (LMC/SMC), also have had an impact on the UFD population. This pair of galaxies constitute \sim 10–15% of the MW’s dark halo mass (e.g., Erkal et al. 2019; Koposov et al. 2023), and they are likely on their first infall into the MW (Besla et al. 2010; Kallivayalil et al. 2013). The LMC and SMC are predicted to have brought their own group of faint satellite galaxies with them (e.g., D’Onghia & Lake 2008; Deason et al. 2015; Jethwa et al. 2016), thus increasing the total number of MW satellites (e.g., Dooley et al. 2017; Newton et al. 2018; Nadler et al. 2020). Evidence of this accreted population can be inferred from the clustering of MW satellites around the LMC and SMC in the Dark Energy Survey (DES) footprint (Koposov et al. 2015a; Drlica-Wagner et al. 2015).

The Magellanic SatelLites Survey¹ (MagLiteS; PI: K. Bechtol) was designed to search for additional satellites near the Magellanic Clouds (Drlica-Wagner et al. 2016), particularly on the southern side of the LMC/SMC that the DES did not cover. Three UFD candidates were discovered with MagLiteS: Pictor II (Pic II), Carina II (Car II), and Carina III (Car III) (Drlica-Wagner et al. 2016; Torrealba et al. 2016a). The radial velocities of Car II and Car III (Li et al. 2018a) suggested they were associated with the LMC based on simulated LMC satellites (Jethwa et al. 2016) and this association was confirmed with full 6-D phase space information from *Gaia* DR2 proper motion measurements (Gaia Collaboration et al. 2016, 2018) and orbit models that included the LMC (Erkal & Belokurov 2020; Patel et al. 2020). Several other UFDs, Horologium I (Hor I), Hydrus I (Hyl I), Phoenix II (Phe II), and Reticulum II (Ret II), have additionally been associated with the LMC (Koposov et al. 2018; Simon 2018; Kallivayalil et al. 2018; Erkal & Belokurov 2020; Patel et al. 2020; Correa Magnus & Vasiliev 2022; Battaglia et al. 2022; Pace et al. 2022; Vasiliev 2023).

The LMC UFD population enables studying UFDs

that formed in a different and lower mass environment compared to the in-situ MW UFDs. Star formation history measurements suggest that the LMC satellites were quenched \sim 600 Myr more recently compared to MW satellites (Sacchi et al. 2021; Durbin et al. 2025). This may be due to patchy reionization allowing lower density environments to form stars longer (e.g., Lunnan et al. 2012; Katz et al. 2020; Kim et al. 2023). Conversely, no difference has been seen in the size-luminosity plane between the LMC and MW UFDs (Richstein et al. 2024) but the number of LMC confirmed UFDs is an order of magnitude smaller than MW UFDs and confirming more LMC UFDs is key to studying environmental differences.

Pic II was identified as a highly probable LMC-associated system due to its close proximity to the LMC ($d_{\text{LMC}} \sim 11$ kpc; Drlica-Wagner et al. 2016), but has not yet been studied spectroscopically. The properties of Pic II are summarized in Table 1. Here we present the first stellar spectroscopy of Pic II to assess its nature and potential association with the LMC. In Section 2, we present our observational data including new Magellan/IMACS (§ 2.1) and Magellan/MIKE (§ 2.2) observations. In Section 3, we derive the systemic properties of Pic II including: updated structural and morphological parameters (§ 3.1), stellar kinematics (§ 3.4), and the spectroscopic metallicity distribution (§ 3.5). In Section 4, we discuss the nature of Pic II (§ 4.1), derive the orbit and discuss the association with the LMC (§ 4.2), discuss the detailed chemical abundances of the brightest star (§ 4.3), and determine the dark matter properties of Pic II (§ 4.4). We summarize our findings in Section 5.

2. DATA

2.1. Medium-resolution spectroscopy: Stellar Kinematics and Metallicities

2.1.1. Target Selection and Observations

Pic II was observed using Inamori Magellan Areal Camera and Spectrograph (IMACS) (Dressler et al. 2006, 2011), a multi-object slit spectrograph at the Magellan Baade 6.5m telescope over 4 observing runs spanning Jan 2017 to Feb 2019. Our observations are summarized in Table 2. We used the same instrument configuration as our previous IMACS observations of UFD galaxy candidates (Simon et al. 2017; Li et al. 2017, 2018a; Simon et al. 2020; Bruce et al. 2023; Cerny et al. 2023a). Specifically, we observed the spectral region 7500–9000 Å at resolution $R \sim 11,000$ and an effective field-of-view of $8' \times 15'$ with the f/4 camera, the 1200/32°7 grating, and a slit width of 0''.7.

Target selection was performed using MagLiteS photometry (Drlica-Wagner et al. 2016). We selected potential members of Pic II as those that lie spatially near the center of Pic II and photometrically near a PARSEC isochrone (Bressan et al. 2012) with $[\text{Fe}/\text{H}] = -2.2$ and age = 12.5 Gyr at distance modulus of $m - M = 18.3$ as measured by Drlica-Wagner et al. (2016). In 2019, we added *Gaia* astrometry to our target selection and included high probability members using the proper motion information provided by *Gaia* DR2 (Gaia Collaboration et al. 2018), using the methods described in Pace & Li (2019).

The IMACS data were reduced as described by Simon et al. (2017) and Li et al. (2017, 2018b), employing a com-

^{*}This paper includes data gathered with the 6.5 meter Magellan Telescopes located at Las Campanas Observatory, Chile.

[†]pvpcale1@gmail.com or apace@virginia.edu

[‡] Galaxy Evolution and Cosmology (GECO) Fellow

¹ MagLiteS was a precursor survey to the DECam Local Volume Exploration survey.

TABLE 1
PHOTOMETRIC AND KINEMATIC PROPERTIES OF PIC II.

Parameter	Description	Pic II	Units	Section
R.A.	R.A. (J2000)	$101.175^{+0.006}_{-0.006}$	deg	3.1
Decl.	Decl. (J2000)	$-59.901^{+0.003}_{-0.003}$	deg	3.1
a_h	Angular semi-major axis length	$2.8^{+0.4}_{-0.3}$	arcmin	3.1
$a_{1/2}$	Physical semi-major axis length	$36.1^{+5.7}_{-4.3}$	pc	3.1
R_h	Azimuthally-averaged angular half-light radius	$2.4^{+0.3}_{-0.3}$	arcmin	3.1
$R_{1/2}$	Azimuthally-averaged physical half-light radius	$32.0^{+4.4}_{-3.6}$	pc	3.1
ϵ	Ellipticity	$0.22^{+0.11}_{-0.13}$		3.1
P.A.	Position angle of major axis (defined east of north)	55^{+20}_{-18}	deg	3.1
$(m - M)_0$	Distance modulus	$18.26^{+0.04}_{-0.03} \pm 0.1$ ^a		3.1
D_\odot	Heliocentric distance	$44.9^{+0.9}_{-0.6} \pm 2.0$ ^a	kpc	3.1
M_V	Absolute (integrated) V-band magnitude	$-2.65^{+0.69}_{-0.48}$	mag	3.1
L_V	V-band luminosity	970^{+630}_{-370}	L_\odot	3.1
M_*	Stellar mass (assuming $M_*/L_V = 2$)	1950^{+1260}_{-750}	M_\odot	3.1
$E(B - V)$	Mean reddening within the half-light radius	0.11	mag	3.1
D_{LMC}	Distance from the LMC	$12.1^{+0.8}_{-0.5}$	kpc	3.1
D_{GC}	Galactocentric distance	$45.6^{+0.9}_{-0.6} \pm 2.0$ ^a	kpc	3.1
\bar{v}_{hel}	Systemic velocity in the heliocentric frame	326.9 ± 1.1	km s^{-1}	3.4
\bar{v}_{gsr}	Systemic velocity in the Galactocentric frame	104.5 ± 1.1	km s^{-1}	3.4
σ_v	Velocity dispersion	$3.5^{+1.1}_{-0.9}$	km s^{-1}	3.4
$M_{1/2}$	Dynamical mass within the half-light radius	$3.6^{+2.9}_{-1.6} \times 10^5$	M_\odot	3.4
M/L	Dynamical mass-to-light ratio within the half-light radius	760^{+910}_{-420}	$M_\odot L_\odot^{-1}$	3.4
[Fe/H]	Mean metallicity from spectroscopic CaT	-2.99 ± 0.06		3.5
$\sigma_{[\text{Fe}/\text{H}]}$	Metallicity dispersion from spectroscopic CaT	< 0.18 ^b		3.5
$\mu_{\alpha*}$	Systemic proper motion in the R.A. direction	$1.18^{+0.05}_{-0.05} \pm 0.023$ ^c	mas yr^{-1}	3.6
μ_δ	Systemic proper motion in the Decl. direction	$1.16^{+0.05}_{-0.05} \pm 0.023$ ^c	mas yr^{-1}	3.6
$C_{\mu_{\alpha*} \times \mu_\delta}$	Correlation between $\mu_{\alpha*}$ and μ_δ	-0.035		3.6
r_{peri}	Orbital pericenter relative to MW	$38.9^{+2.5}_{-3.0}$	kpc	4.2
r_{apo}	Orbital apocenter relative to MW	219^{+99}_{-54}	kpc	4.2
e	Orbital eccentricity relative to MW	$0.70^{+0.09}_{-0.08}$		4.2
$r_{\text{peri, LMC}}$	Orbital pericenter relative to the LMC	$7.8^{+4.4}_{-3.4}$	kpc	4.2
$r_{\text{apo, LMC}}$	Orbital apocenter relative to the LMC	$29.9^{+9.7}_{-6.0}$	kpc	4.2
e_{LMC}	Orbital eccentricity relative to the LMC	$0.62^{+0.16}_{-0.16}$		4.2
p_{LMC}	Fraction of orbits bound to the LMC	0.91		4.2
$\log_{10} J(0^\circ 2)$	Integrated J-factor within a solid angle of $0^\circ 2$	18.33 ± 0.53	$\log_{10} \text{GeV}^2 \text{ cm}^{-5}$	4.4
$\log_{10} J(0^\circ 5)$	Integrated J-factor within a solid angle of $0^\circ 5$	18.48 ± 0.55	$\log_{10} \text{GeV}^2 \text{ cm}^{-5}$	4.4

NOTE. —

^a A systematic error of 0.1 is included in the distance modulus which corresponds to a systematic error of ~ 2 kpc in the heliocentric and Galactocentric distance.

^b Upper limits listed here are at the 95% credible level.

^c The last term corresponds to the systematic proper motion error from Lindegren et al. (2021).

TABLE 2
SUMMARY OF IMACS OBSERVATIONS.

MJD ^a	Run	Mask	R.A. (h:m:s)	Decl. (d:m:s)	$\sum t_{\text{exp}}$ (s)	Seeing	# targets	# useful ^b
57779.17	Jan 2017	Pic2_mask1	06:44:50.000	-59:54:15.00	14400	1''5	45	37
58103.53	Dec 2017	Pic2_mask2	06:44:45.100	-59:55:22.00	34200	0''65-1''25	40	27
58104.13	Dec 2017	Pic2_mask3	06:44:50.000	-59:53:35.00	9600	0''75	26	19
58499.11	Jan 2019	Pic2_mask4	06:44:32.000	-59:57:00.00	9000	0''6-1''1	19	19
58526.54	Feb 2019	Pic2_mask5	06:44:13.800	-59:47:00.00	7346	0''65-2''0	13	10

^a The MJD presented is the average over multiple nights of a single run (where applicable).

^b The number of observed spectra with a reliable radial velocity measurement.

bination of the Cosmos reduction pipeline (Dressler et al. 2011; Oemler et al. 2017) and a version of the DEEP2 data reduction pipeline (Cooper et al. 2012; Newman et al. 2013) adapted for IMACS. In order to keep the temporal information to check binarity as well as to check potential systematics, we only coadded spectra taken with the same mask and within a given < 3 night run.

2.1.2. Velocity and Metallicity Measurements

The line-of-sight velocity and metallicity measurements follow the same method as described in other papers by our group (e.g., Li et al. 2017, 2018a,b). Specifically, the velocities are derived via template fitting with a Markov chain Monte Carlo sampler; and the metallicities are derived by measuring the equivalent widths (EWs) of the Calcium Triplet (CaT) lines around 8500 Å using the calibration from Carrera et al. (2013). Spectra with signal-to-noise > 5 ($S/N > 9$) usually have good velocity (metallicity) measurements. Successful velocities and metallicities are presented in Table 3 and per-mask measurements are included in the zenodo repository². In total, we observed 143 targets with 112 good quality velocity measurements of 94 unique stars. We obtained 99 good quality CaT EW measurements of 84 unique stars.

For our primary analysis, we combined repeat measurements at the catalog level. For the combined velocities we fit a free velocity and dispersion to the repeat measurements and use the mean velocity and error for the star's intrinsic properties. This method has the appealing limits that it will match the variance of the weighted mean for the velocity error for non-variable sources (the expected behavior for non-variable sources with errors that are Normally distributed) and will have larger errors for stars that have evidence of variability. This combination method can be more robust to unidentified binary stars as stars with variation will have larger errors (Buttry et al. 2022). In principle, the center-of-mass velocity for binary stars should be used but this is extremely difficult to correctly identify with only a few velocity measurements. For repeat metallicity measurements we combine measurements with the weighted mean and variance of the weighted mean for the combined error. We have verified that using the best measurement (highest signal-to-noise) instead of the combined value gives similar results (when excluding binary stars).

2.2. High-resolution spectroscopy: Chemical Abundance Analysis

2.2.1. Observations and Radial Velocity

We obtained Magellan Inamori Kyocera Echelle (MIKE) spectra (Bernstein et al. 2003) at the Magellan Clay 6.5 m telescope of star 10286300071032³, hereafter PicII-1, the brightest known member of Pic II ($G \sim 17.05$), on 2017 December 06. We used the 1''.0 slit which has a spectral resolution of $R \sim 28,000$ and 22,000 in the blue and red arms, respectively. We obtained 3 x 2700s exposures with 2x2 binning, resulting in S/N per pixel ~ 14 at 4250Å and ~ 35 at 6000Å. Data were reduced using the standard MIKE pipeline in CarPy (Kelson 2003)⁴.

² <https://doi.org/10.5281/zenodo.15706700>

³ Gaia DR3 source_id = 5480249356255194112

We analyzed the spectrum using the 2017 version of the 1D LTE radiative transfer code MOOG (Sneden 1973) updated to include opacity from scattering (Sobeck et al. 2011; Sobeck & Sneden 2023)⁵. We used the alpha-enhanced plane-parallel Castelli & Kurucz (2003) (ATLAS) model atmospheres. Normalization, radial velocity correction, equivalent width measurements, and spectral synthesis fitting was done with smhr⁶, first described in Casey (2014).

The radial velocity was determined following Ji et al. (2020b). Each MIKE spectral order from 3700Å-6800Å was cross-correlated against a rest frame spectrum of the metal-poor red giant HD122563. As velocity uncertainties are dominated by wavelength calibration issues, we adopt the order-to-order scatter as the velocity uncertainty. The final velocity is $v_{\text{hel}} = 331.0 \pm 1.0 \text{ km s}^{-1}$. Separately, our IMACS data found PicII-1 to have velocities 330.0, 328.2, 329.9 km s^{-1} , each with uncertainty 1 km s^{-1} . There is no evidence for large radial velocity variations for PicII-1.

2.2.2. Stellar Parameters and Abundances

Stellar parameters were determined following the procedure in Frebel et al. (2013), i.e. excitation, ionization, and line strength balance of Fe lines with an empirical correction to match a photometric temperature scale. We find $T_{\text{eff}} = 4520 \pm 174 \text{ K}$, $\log g = 0.80 \pm 0.37$, $\nu_t = 2.07 \pm 0.22 \text{ km s}^{-1}$, and $[\text{Fe}/\text{H}] = -3.27 \pm 0.22$ for the effective temperature, surface gravity, microturbulence velocity, and metallicity, respectively. The uncertainties include statistical error from the Fe lines as well as systematic uncertainties of 150 K, 0.3 dex, and 0.2 km s^{-1} for T_{eff} , $\log g$, and ν_t respectively that reflect scatter in the Frebel et al. (2013) calibration. Line lists were adopted from Ji et al. (2020b). Abundances of most elements were determined from equivalent widths, but for the following features we determined the abundance with spectral synthesis: molecular CH bands; hyperfine structure in Sc, Mn, Co; and Al and Si lines somewhat blended with CH. We only use lines with $\lambda > 4000\text{\AA}$ because the S/N is too low at bluer wavelengths (< 8 per pixel). The exception is a strong Al line at 3944Å as no other Al lines are available: this line is clearly detected, but given the S/N the abundance is extremely uncertain (constraint no better than 0.5 dex). We also determined formal 5σ upper limits for Sr, Ba, and Eu using spectral synthesis of the 4215Å, 4934Å, and 4129Å lines, respectively (see Ji et al. 2020a for more details).

Final abundances and uncertainties of PicII-1 are given in Table 4. For each element, N is the number of lines measured. $\log \epsilon(X)$ is the average abundance of those lines weighted by the abundance uncertainty. If $\log \epsilon_i$ and σ_i are the abundance and uncertainty of line i , then we define $w_i = 1/\sigma_i^2$ and $\log \epsilon(X) = \sum_i (w_i \log \epsilon_i) / \sum_i w_i$. The uncertainty σ_i for an individual line is found by propagating spectrum noise uncertainty. σ is the standard deviation of those lines (undefined if one line). σ_w accounts for the abundance uncertainty due to propagating individual line uncertainties, i.e. $1/\sigma_w^2 = \sum_i w_i$

⁴ <http://code.obs.carnegiescience.edu/mike>

⁵ <https://github.com/alexfji/moog17scat>

⁶ <https://github.com/andycasey/smhr>

TABLE 3
PROPERTIES OF SPECTROSCOPICALLY CONFIRMED MEMBER STARS OF PIC II

ID	Gaia DR3 source_id	RA (deg)	DEC (deg)	g_0 (mag)	r_0 (mag)	v_{hel} (km s $^{-1}$)	$\Sigma \text{EW CaT}$ (Å)	[Fe/H] (dex)
10286300071032	5480249356255194112	101.22791	-59.91751	17.48	16.75	329.4 \pm 0.6	1.92 \pm 0.12	-3.08 \pm 0.08
10286300171312	5480252100736880640	101.07264	-59.92858	19.03	18.51	327.1 \pm 0.6	1.46 \pm 0.11	-3.06 \pm 0.09
10286300169004	5480170908676338432	100.89608	-59.88540	19.19	18.71	320.5 \pm 1.6	1.61 \pm 0.60	-2.91 \pm 0.41
10286300346714	5480248011928003968	101.28227	-59.97635	18.91	19.05	330.8 \pm 1.4		
10286300169363	5480252444334270080	101.20003	-59.89651	18.86	19.08	331.0 \pm 1.9		
10286300169338	5480252276833093248	101.15539	-59.89063	19.76	19.28	327.4 \pm 0.9	1.41 \pm 0.17	-2.94 \pm 0.14
1028630001346	5480252066377147008	101.17612	-59.90296	20.08	19.63	325.3 \pm 1.1	1.53 \pm 0.24	-2.79 \pm 0.19
10286300417761	5480158092493302272	100.94904	-59.97386	20.38	19.92	328.7 \pm 1.5	1.21 \pm 0.28	-3.00 \pm 0.28
10286300169343	5480252341255057536	101.15827	-59.88901	20.41	19.97	326.9 \pm 1.7	1.42 \pm 0.44	-2.82 \pm 0.36
10286300001343	5480252276831909376	101.17167	-59.89087	20.70	20.25	329.1 \pm 7.5	1.35 \pm 0.20	-2.74 \pm 0.18
10286300071017	5480247840129310848	101.18892	-59.98813	20.89	20.45	317.0 \pm 2.4		
10286300300125	5480249008361992448	101.15214	-59.94265	20.96	20.53	330.9 \pm 2.7		
10286300171369		101.10710	-59.94019	21.51	21.13	326.0 \pm 2.3	1.02 \pm 0.81	-2.81 \pm 0.73

NOTE. — Pic II spectroscopic members ordered by increasing r-band magnitude. Details of each parameter can be found in Section 2.1. The full spectroscopic sample along with additional columns can be found at the following zenodo repository: <https://doi.org/10.5281/zenodo.15706700>

(McWilliam et al. 1995). [X/H] is the abundance relative to solar abundances from Asplund et al. (2009). [X/Fe] is calculated using either [Fe I/H] or [Fe II/H], depending on whether X is neutral or ionized. σ_{XH} is the quadrature sum of σ/\sqrt{N} , σ_w , and abundance uncertainties due to 1σ stellar parameter variations. σ_{XFe} is similar to σ_{XH} , but when calculating the stellar parameter uncertainties we include variations in Fe. We use the difference in Fe I abundance for neutral species and the difference in Fe II abundance for ionized species to calculate this error. The [X/Fe] error is usually smaller than the [X/H] error, since abundance differences from changing T_{eff} and $\log g$ usually affect X and Fe in the same direction.

2.3. DELVE photometry

We utilize data from the DECam Local Volume Exploration Survey (DELVE; Drlica-Wagner et al. 2021), a southern sky survey performed with DECam (Flaugher et al. 2015) on the 4-m NSF Víctor M. Blanco Telescope at the NSF Cerro Tololo Inter-American Observatory (CTIO). For this analysis, we used the stellar catalog from the upcoming Third Data Release (DR3) of DELVE (Drlica-Wagner, DELVE Collaboration in prep.), which utilizes the DES Data Management data processing pipeline (Morganson et al. 2018) as described by Tan et al. (2025) and Anbjagane et al. (2025). The data release covers \sim 14,000 deg 2 of the sky with a median limiting magnitude of $g \sim 24.1$, $r \sim 23.6$, $i \sim 23.2$, $z \sim 22.5$ (estimated at S/N = 10 in 2" aperture) and the DELVE catalog contains the MagLiteS observations used to discover Pic II. The DECam data were processed through the image coaddition pipeline closely following the procedure described for DES DR2 (Abbott et al. 2021). The survey uses SourceExtractor to perform object detection on the $r + i + z$ detection coadd image, with a detection threshold of $\sim 5\sigma$. We use photometry derived using multi-epoch PSF model fits which are obtained using fitvd (Hartley et al. 2022). fitvd obtained fluxes for each detected source by fitting individual-epoch PSF models at the individual constituent images that went into the coadd at the object's location. For star-

galaxy separation we use $0 \leq \text{EXT_FITVD} \leq 2$ (Bechtol et al. 2025). We note the photometry presented in this paper is corrected for extinction using the $E(B - V)$ values from the reddening map of Schlegel et al. (1998) with the correction from Schlafly & Finkbeiner (2011). We find the mean reddening within the half-light radius of Pic II to be $E(B - V) = 0.11$.

2.4. MAGIC Metallicity Sensitive Narrowband Photometry

Pic II was imaged with the narrow-band N395 filter on DECam as part of the Mapping the Ancient Galaxy in CaHK Survey (DECam MAGIC; Chiti et al., in prep) with NOIRLab Prop. ID 2023B-646233. The N395 filter includes the Ca II H and K lines at 3968.5 Å and 3933.7 Å, respectively, similar to other metallicity-sensitive filters (e.g., the Pristine survey; Starkenburg et al. 2017), allowing the derivation of reasonably precise metallicities ($\sigma_{[\text{Fe}/\text{H}]} \sim 0.16$; Barbosa et al. 2025) for individual stars through photometry. Specifically, MAGIC obtained 3×12 min exposures that were dithered and centered on Pic II on the night of February 7th, 2024⁷. More details on the processing and photometric metallicities will be presented in Chiti et al., (in prep), but we refer the reader to Barbosa et al. (2025) for an overview and early result from the MAGIC survey. In particular, see Figure 4 of Barbosa et al. for metallicity error calibration. Specific to this work, we use this narrow-band CaHK data to verify the metal-poor nature of Pic II members as an additional check on their membership. Lastly we note that the MAGIC catalog uses DELVE DR2 photometry for the metallicity derivation and future MAGIC catalogs will utilize the upcoming DELVE DR3 (Drlica-Wagner et al. 2022).

2.5. Gaia Astrometry

We use Gaia DR3 astrometry (Lindegren et al. 2021; Gaia Collaboration et al. 2023) to assist in Pic II membership and to measure the systemic

⁷ Our analysis uses the internal MAGIC version v250130

TABLE 4
ABUNDANCES OF PICII-1

El.	<i>N</i>	$\log \epsilon(X)$	σ_w	σ	[X/H]	σ_{XH}	[X/Fe]	σ_{XFe}
CH	2	4.80	0.04	0.04	-3.63	0.48	-0.36	0.21
Na I	1	3.96	0.06	...	-2.28	0.27	0.99	0.12
Mg I	5	5.24	0.07	0.15	-2.36	0.23	0.91	0.10
Al I	1	2.82	-3.63	...	-0.36	...
Si I	2	4.87	0.20	0.12	-2.64	0.44	0.64	0.21
K I	2	2.89	0.04	0.03	-2.14	0.17	1.13	0.07
Ca I	8	3.47	0.06	0.15	-2.87	0.15	0.40	0.10
Sc II	7	0.46	0.09	0.09	-2.69	0.18	0.59	0.18
Ti II	18	2.15	0.04	0.14	-2.80	0.15	0.48	0.08
Cr I	5	2.15	0.09	0.16	-3.49	0.25	-0.22	0.10
Mn I	2	1.04	0.18	0.18	-4.39	0.34	-1.12	0.19
Fe I	96	4.23	0.02	0.22	-3.27	0.21
Fe II	11	4.22	0.07	0.21	-3.28	0.14
Co I	2	1.81	0.11	0.11	-3.18	0.29	0.09	0.13
Ni I	1	2.71	0.11	...	-3.51	0.24	-0.24	0.12
Sr II	1	< -2.06	< -4.93	...	< -1.65	...
Ba II	1	< -2.68	< -4.86	...	< -1.58	...
Eu II	1	< -2.05	< -2.57	...	< 0.71	...

NOTE. — ID=10286300071032 and Gaia DR3 source_id = 5480249356255194112. The Al abundance has an uncertainty > 0.5 dex. The CH abundance has not been corrected for the star's evolutionary status here, but the correction is +0.73 dex (Placco et al. 2014).

proper motion of Pic II. We apply the following cuts to select stars with good quality astrometry: `astrometric_params_solved > 3`, `ruwe < 1.4`, and `astrometric_excess_noise_sig < 2` (following Lindegren et al. 2021; Pace et al. 2022).

3. SYSTEMIC PROPERTIES OF PIC II

3.1. Updated Morphological Parameters

DELVE DR3 photometry extends roughly a magnitude fainter than the discovery analysis (Drlica-Wagner et al. 2016) and will provide significantly improved constraints on the structural and morphological parameters of Pic II. We use the `ugali` toolkit⁸ (Bechtol et al. 2015; Drlica-Wagner et al. 2015, 2020) to update the morphological parameters. Briefly, `ugali` simultaneously fits the structural and stellar population parameters of a UFD. The structural component is fit with a Plummer (1911) profile and the free parameters are: centroid coordinates ($\alpha_{\text{J2000}}, \delta_{\text{J2000}}$), semi-major axis (a_h), ellipticity (ϵ), position angle (P.A.) of the major axis (defined east of north). The magnitude and colors are fit with PARSEC stellar isochrones (Bressan et al. 2012; Chen et al. 2014; Tang et al. 2014; Chen et al. 2015) with the following free parameters: distance modulus ($m - M)_0$, age (τ), and metallicity (Z_{phot}). The model lastly includes a parameter for the stellar richness (λ), which normalizes the total number of stars in the system (Drlica-Wagner et al. 2020). We use `emcee` (Foreman-Mackey et al. 2013) to simultaneously fit all parameters in the model. The posteriors from the `ugali` fits are summarized in Table 1.

We find an azimuthally averaged half-light radius of $R_{1/2} \sim 32$ pc, an ellipticity of $\epsilon \sim 0.22$, an absolute *V*-band magnitude of $M_V \sim -2.6$, and a distance modulus of $(m - M)_0 = 18.45$ or $D_\odot = 45$ kpc. To compute the *V*-band magnitude of Pic II, we convert from *g*, *r* mag-

nitudes using the relation in Abbott et al. (2021). Compared to the discovery paper (Drlica-Wagner et al. 2016), the centroid is offset by $\approx 17''$, the size is 25% smaller ($R_{1/2} \sim 32$ pc vs $R_{1/2} \sim 43$ pc), the luminosity is 30% lower ($M_V \sim -2.6$ versus $M_V \sim -3.2$), and shape and orientation are better constrained. Our updated morphological parameter measurements are broadly consistent within the uncertainties of the discovery analysis (Drlica-Wagner et al. 2016). With our updated size and luminosity measurement, Pic II remains larger than known globular clusters and ambiguous systems and has properties similar to other MW and LMC UFDs.

3.2. Spectroscopic Membership Classification

We assess the membership of each star based off its kinematics, chemistry, and photometric properties. We note that “background” stars here can refer to either foreground MW stars or LMC stars at a similar distance. The properties of the spectroscopic sample are summarized in Figure 1. We highlight our final spectroscopic sample, along with clear background stars, and background stars with a velocity similar to Pic II but classified as non-members. The velocity distribution of our spectroscopic sample has two peaks, a wide peak at ~ 50 km s $^{-1}$ which we associate with the MW and a second narrow peak at $v_{\text{hel}} \sim 330$ km s $^{-1}$ which we associate as Pic II. The majority of the stars closest to Pic II match the $v_{\text{hel}} \sim 330$ km s $^{-1}$ peak and the velocity association is further confirmed by selecting on proper motion. The proper motion selection can be done with the membership from *Gaia* proper motion based mixture models (Battaglia et al. 2022; Pace et al. 2022) or a proper motion and parallax selection such as the membership score from Tolstoy et al. (2023). All proper motion selections uncover the same velocity peak which confirms the Pic II systemic velocity.

While the majority of the background peaks at

⁸ <https://github.com/DarkEnergySurvey/ugali>

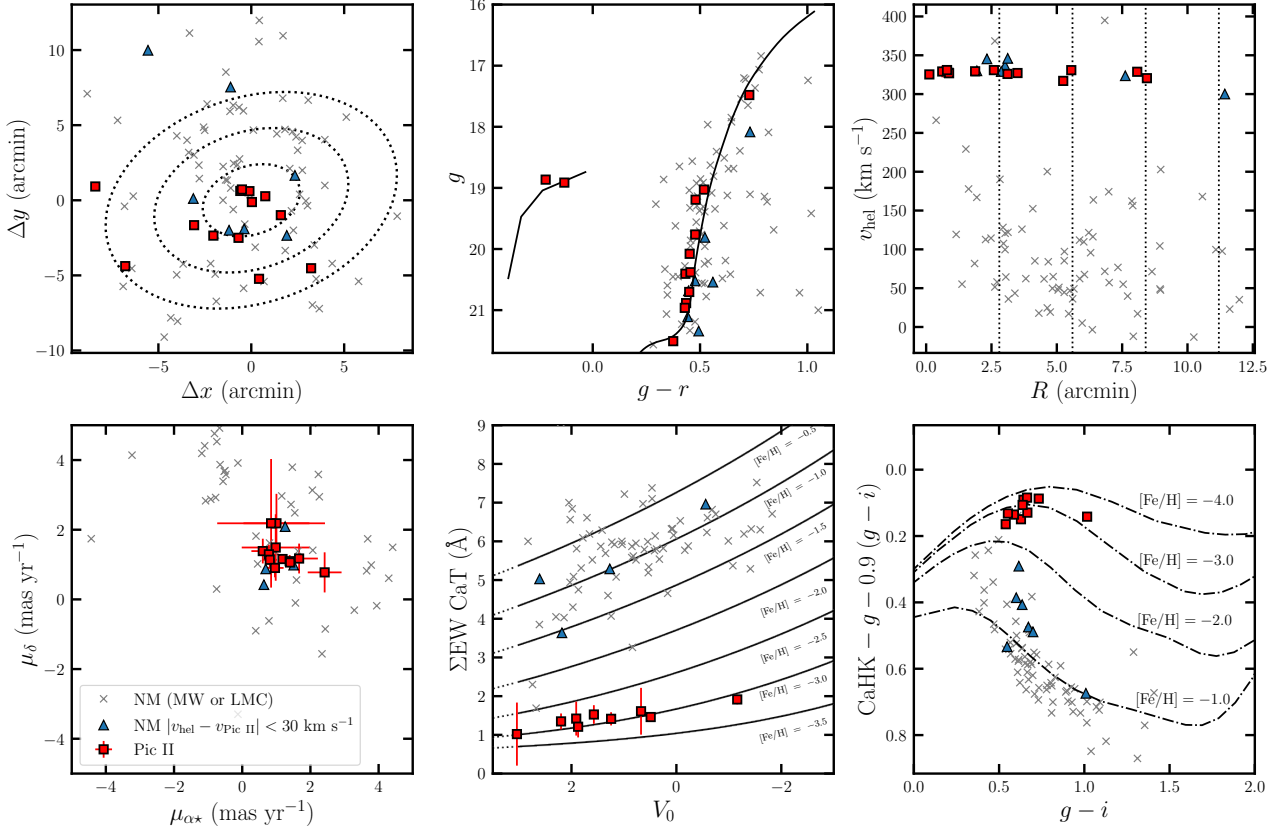


FIG. 1.— Chemo-dynamic properties of the Pic II spectroscopic sample. Pic II members are shown in red squares while non-members with a velocity near Pic II are in blue triangles ($|v_{\text{hel}} - v_{\text{Pic II}}| < 30 \text{ km s}^{-1}$) and the remainder of the non-members are shown in gray x's (NM in legend). **Upper-left:** spatial position of the sample relative to the center of Pic II. Dotted ellipses correspond to $1, 2, 3 \times R_h$. **Upper-middle:** DELVE DR2 color-magnitude diagram ($g - r$ vs g). We include an old, metal-poor red-giant branch isochrone (age = 12.5 Gyr; $Z=0.0001$) from Dotter et al. (2008) and the blue-horizontal branch track of the old, metal-poor globular cluster M92 scaled to the distance of Pic II. **Upper-right:** projected radius (R) vs heliocentric velocity (v_{hel}). Dotted vertical lines are multiples of the half-light radius. **Lower-left:** Vector point diagram ($\mu_{\alpha*}$ vs μ_{δ}). **Lower-middle:** V-band absolute magnitude vs Calcium Triplet (CaT) equivalent width. Lines of constant [Fe/H] from Carrera et al. (2013) are overlaid. Note that the V-band absolute magnitude assumes the Pic II distance modulus and only Pic II members will have the correct absolute magnitude. Regardless, there is a clear difference in the equivalent width between Pic II members and MW/LMC foreground stars. **Lower-right:** metallicity-sensitive color-color diagram with MAGIC CaHK photometry. Lines of constant [Fe/H] with $\log g = 2$ are overlaid. Similar to the CaT equivalent width, there is a clear difference in color between Pic II members and the foreground stars.

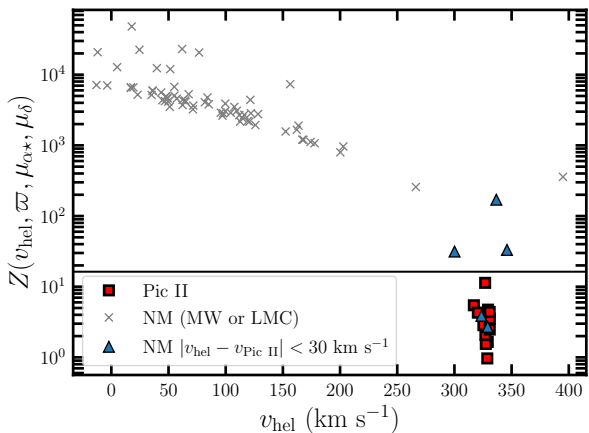


FIG. 2.— Membership score (Tolstoy et al. 2023) for stars in our spectroscopic sample. The horizontal line at 16.2 corresponds to a 3σ cut for selecting members. The colors and markers are the same as Figure 1.

50 km s^{-1} there is a tail beyond $\sim 200 \text{ km s}^{-1}$ that we associate with the LMC. The velocity at the center of the LMC is $v_{\text{hel}} = 262 \pm 3.4 \text{ km s}^{-1}$ (van der Marel et al. 2002) and at the position of Pic II, the LMC velocity is $v_{\text{hel}} \approx 300 \text{ km s}^{-1}$ (see Figure 3 of van der Marel & Kallivayalil 2014). We note the excess of stars near the Pic II systemic velocity that are non-members and these stars have kinematics that are consistent with the broad LMC distribution. As Pic II is a likely LMC satellite (see Section 4.2), it is not surprising to see some overlap with the LMC foreground. We note that LMC stars have been found in the foreground of other dwarf galaxies including Carina (Muñoz et al. 2006) and Carina II (Li et al. 2018a).

Our final membership selection also considers metallicity, derived both from the spectroscopic CaT equivalent width and the CaHK photometry, and the location on an old, metal-poor isochrone (Dotter et al. 2008, age=12.5 Gyr and $Z=0.0001$). The lower-middle panel of Figure 1 compares the absolute V-band magnitude with the spec-

troscopic CaT equivalent width. Overlaid are lines of constant [Fe/H] from Carrera et al. (2013). The spectroscopic members have much lower equivalent widths than the background stars. We present a color-color diagram in CaHK – $g - 0.9$ ($g - i$) vs. $g - i$ space in the lower-right hand panel of Figure 1, which has been established to define axes where metal-poor and metal-rich stars separate from each other (e.g., Keller et al. 2007; Starkenburg et al. 2017; Chiti et al. 2020; Huang et al. 2022). As expected, we find that our spectroscopic members of Pic II appear more metal-poor than MW halo stars in this plot, adding confidence to their membership. For completeness, we note that the g, i photometry in this metallicity-sensitive color-color plot is from DELVE DR2, and that iso-metallicity contours from a grid of Turbospectrum-generated synthetic spectra at $\log g = 2$ dex are overplotted (Chiti et al. 2020; Barbosa et al. 2025).

To quantitatively assess membership, we compute the membership score (Tolstoy et al. 2023). The membership score is effectively a 3σ selection around the systemic properties with either proper motion and parallax, Z_3 , or proper motion, parallax, and velocity, Z_4 . Members are identified within $Z_4 < 16.3$ (the 3σ limit for a 4-dimensional χ^2 distribution) and we show the membership score of all stars in Figure 2. All members previously identified satisfy this quantitative selection.

Of the non-members within 30 km s^{-1} of the Pic II velocity (green points in Figure 1), five stars are clear astrometric non-members and two stars have a metallicity (either CaT EW or CaHK colors) that is much larger than Pic II. Both of the metallicity outlier stars are consistent with the velocity and proper motion of Pic II and have $Z_4 < 16.3$. The first, (ID=10286300169398), has $[\text{Fe}/\text{H}]_{\text{CaT}} = -1.53 \pm 0.15$ and is 1.2 dex more metal-rich than any of the Pic II members. This star does not have a $[\text{Fe}/\text{H}]_{\text{CaHK}}$ in the MAGIC catalog but is located in the CaHK color space near this metallicity. Lastly, we note this star is located on the old, metal-poor stellar isochrone. While a $[\text{Fe}/\text{H}] \sim -1.5$ star in a UFD is not uncommon or implausible a large metallicity gap seems unlikely and we consider this star a likely LMC interloper. The second, (ID=10286300169327), does not have a CaT EW measurement and has $[\text{Fe}/\text{H}]_{\text{CaHK}} = -1.2$. This star is redder than the stellar isochrone. As this star is even more metal-rich it is even less likely to be a Pic II member. In total, we identify 13 Pic II members, which includes two horizontal branch stars.

The spatial distribution of the spectroscopic member sample in Figure 1 is quite asymmetric and nearly all the members are located on the southern side of Pic II (all spectroscopic members are at $y < 1'$). Obtaining this distribution by chance is unexpected and there are more successful velocity measurements on the northern side ($y > 0$; N=63) than the southern side ($y < 0$; N=49) of Pic II. This asymmetry is partly caused by the presence of a nearby relatively bright star ($G \sim 9.4$) that is located $2'$ from the center of Pic II and there are only a few sources within $\approx 1'$ of this star in our photometric catalogs. Two of our five masks utilize *Gaia* astrometry to target high priority targets missing from past observations. Neither of these masks targeted the northern central side of Pic II. There are additional unobserved

high-probability *Gaia* candidates (Battaglia et al. 2022) that are outside our *Gaia* target selection (three high probable candidates are near the bright star) and if these stars were confirmed as members, the spectroscopic sample would become more symmetric. Overall, we suspect that our spectroscopic target selection and the presence of a nearby bright star is the cause of at least some the asymmetric spectroscopic member distribution.

3.3. Constraints on Binarity

Almost half of the Pic II spectroscopic members have repeat velocity measurements. Of the 6 members with repeat measurements, only one star, ID=10286300001343⁹, shows clear evidence for velocity variations. From the repeat measurements, this star has a reduced χ^2 of ≈ 63 with a probability of $P(\chi^2, n = 4) \approx 10^{-13}$ that the measurements are drawn from a constant velocity distribution and it is highly likely to be a binary star. All other stars with repeat measurements do not show evidence for velocity variation. Due to the low number of epochs (there are four velocity measurements but 2 epochs are 1 day apart), we are not able to constrain any binary orbital parameters.

3.4. Stellar Kinematics

We assume the velocity distribution follows a Normal distribution and use an unbinned likelihood to compute the systemic velocity and velocity dispersion (e.g., Walker et al. 2006). We use a Jeffreys prior for the velocity dispersion ($-2 \leq \log_{10} \sigma_v \leq 1.7$), and from the 13 spectroscopic member sample we find $\bar{v}_{\text{hel}} = 326.9 \pm 1.1 \text{ km s}^{-1}$ and $\sigma_v = 3.5^{+1.1}_{-0.9} \text{ km s}^{-1}$. If we assume a linear prior in the velocity dispersion ($0 \leq \sigma_v \leq 20$) we find $\bar{v}_{\text{hel}} = 327.0 \pm 1.2 \text{ km s}^{-1}$ and $\sigma_v = 3.8^{+1.3}_{-0.9} \text{ km s}^{-1}$. Including or excluding the binary star does not affect our inferred stellar kinematics due to the large velocity error for the combined velocity measurement for this star ($v_{\text{hel}} = 329.1 \pm 7.5 \text{ km s}^{-1}$).

To assess the significance of resolving the velocity dispersion, we compute the Bayes factor (B) comparing a free velocity dispersion model and zero velocity dispersion model. The Bayes factor is the ratio of Bayesian evidence between two models and is a commonly utilized model selection tool (see Trotta 2008, for a review). We use the pocoMC package (Karamanis et al. 2022a,b) to sample the posterior distributions and compute the Bayesian evidence for both models. We find $\ln B = 12.1$ strongly favoring the non-zero dispersion model¹⁰. We use Jeffreys' scale to interpret the Bayes factor where values of $\ln B < 1$, $1\text{--}2.5$, $2.5\text{--}5$, > 5 correspond to inconclusive, weak, moderate, and strong evidence in favor of one model, respectively (negative value favor the other model) (Trotta 2008). Overall, we find strong evidence for a non-zero velocity dispersion.

To assess the robustness of the velocity dispersion to outliers, we perform a jackknife test. This test recomputes the velocity dispersion by excluding one star at a time. There are two stars (ID = 10286300169004,

⁹ Gaia DR3 source_id=5480252276831909376

¹⁰ The Bayes factor drops to 11.9 if we compare to the stellar only velocity dispersion of 0.18 km s^{-1} which still strongly favors the velocity dispersion model. For the linear prior we find $\ln B = 12.4$ comparing to the zero dispersion model.

10286300071017) that when excluded decrease the velocity dispersion to $\sim 2.5 \text{ km s}^{-1}$ from $\sim 3.5 \text{ km s}^{-1}$ and if both are removed the velocity dispersion becomes marginally unresolved (the posterior peaks at $\sim 1.2 \text{ km s}^{-1}$ but there is a tail in the posterior distribution consistent with zero velocity dispersion). Neither star has a repeat velocity measurement and both are likely members given either *Gaia* astrometry or a metallicity measurement¹¹. It is possible that either or both are binary stars but further radial velocity measurements are required to test binarity.

Unresolved binary stars can inflate the inferred velocity dispersion (e.g., Minor et al. 2010; McConnachie & Côté 2010; Buttry et al. 2022). To assess the impact the identified binary could have had on the stellar kinematics without our multi-epoch data, we recompute the velocity dispersion using the first epoch velocity measurement instead of the combined velocity ($v_{\text{first epoch}} = 346.8 \pm 2.8 \text{ km s}^{-1}$). The binary-influenced stellar kinematics are $\bar{v}_{\text{hel}} = 328.1 \pm 1.8 \text{ km s}^{-1}$ and $\sigma_v = 6.3^{+1.8}_{-1.3} \text{ km s}^{-1}$. While the inferred velocity dispersion is almost twice as large, the binary star may not have been considered a member as it is a 4.5σ velocity outlier (with $\sigma_v = 3.5 \text{ km s}^{-1}$). Without the multi-epoch velocity data the velocity dispersion of Pic II could have been inflated similar to Boötes II and Triangulum II (Kirby et al. 2017; Bruce et al. 2023).

We compute the dynamical mass and mass-to-light ratio of Pic II with the mass estimator from Wolf et al. (2010). We note this estimator computes the dynamical mass within the 3D half-light radius ($r_{1/2}$) which is slightly larger than the projected half-light radius for a Plummer profile ($r_{1/2} \approx 4/3R_{1/2}$). From the velocity dispersion measurement here and the half-light radius, distance, luminosity measurements in Section 3.1, we infer $M_{1/2} = 3.6^{+2.9}_{-1.6} \times 10^5 \text{ M}_\odot$ and $M/L = 760^{+910}_{-420} \text{ M}_\odot/\text{L}_\odot$. The high dynamical mass-to-light ratio implies that Pic II is a dark matter-dominated system.

A velocity gradient is a clear sign of disequilibrium and has been searched for in many UFDs (e.g., Martin & Jin 2010; Collins et al. 2017; Li et al. 2018b; Ou et al. 2024). The velocity gradient model adds two additional parameters, the magnitude of the velocity gradient (v_g), and its direction (θ_g). With our stellar-kinematic sample we measure an upper limit of $v_g < 1.3 \text{ km s}^{-1} \text{ arcmin}^{-1}$ for the velocity gradient (95% credible level). With the majority of the spectroscopic sample located on the southern side of Pic II, the small sample size, and the angular extent of the data, measuring a non-detection is not surprising.

3.5. Metallicity Dispersion

We apply the same likelihood analysis to determine the mean metallicity and metallicity dispersion of Pic II assuming that the metallicity distribution of Pic II is a Normal distribution (with a Jeffreys prior for the metal-

licity dispersion). From the nine RGB members with good quality CaT measurements, we obtain $\overline{[\text{Fe}/\text{H}]} = -2.99 \pm 0.06$ and $\sigma_{[\text{Fe}/\text{H}]} < 0.18$ (95% credible level). Using a linear prior instead for the metallicity dispersion, we find $\sigma_{[\text{Fe}/\text{H}]} < 0.27$ (95% credible level).

To verify our results, we apply the same analysis to the photometric CaHK metallicity. There are ten RGB spectroscopic members with photometric metallicity measurements and we determine the metallicity distribution to be $\overline{[\text{Fe}/\text{H}]}_{\text{CaHK}} = -2.98 \pm 0.10$ and $\sigma_{[\text{Fe}/\text{H}]}_{\text{CaHK}} < 0.35$ (95% credible level). The $[\text{Fe}/\text{H}]$ measurements with both spectroscopic CaT and photometric CaHK agree and infer that Pic II is an extremely metal-poor system with a small (unresolved) metallicity dispersion.

We apply the same Bayes factor significant test to the metallicity to assess whether the metallicity dispersion is resolved. For linear priors, we find $\ln B = -1.7, -0.4$ for the CaT and CaHK $[\text{Fe}/\text{H}]$ measurements, respectively, and for Jeffreys priors we find $\ln B = -0.5, 0.1$ for the CaT and CaHK $[\text{Fe}/\text{H}]$ measurements, respectively. In general, we do not find evidence for a non-zero metallicity dispersion and either a larger sample and/or more precise metallicity measurements are required to resolve the dispersion.

As discussed in Section 3.2, there are two more metal-rich stars that have a velocity and proper motion consistent with Pic II. If we include the more metal-poor star of the two (ID=10286300169398; $[\text{Fe}/\text{H}]_{\text{CaT}} \sim -1.5$) in the metallicity distribution calculation, we find $\overline{[\text{Fe}/\text{H}]}_{\text{CaT}} = -2.76^{+0.18}_{-0.17}$ and $\sigma_{[\text{Fe}/\text{H}]}_{\text{CaT}} = 0.49^{+0.16}_{-0.11}$. These values are consistent with other UFD galaxies. Due to the large metallicity gap between this star and the current most metal-rich Pic II star (~ -2.7), we do not consider this star a member.

The brightest member star in Pic II has a CaT metallicity of $[\text{Fe}/\text{H}] = -3.08 \pm 0.08$ and is further observed with high-resolution spectroscopy discussed in Section 4.3.

3.6. Systemic Proper Motion

As shown in Figure 1, all 12 spectroscopic members with *Gaia* astrometry cluster nicely around $(\mu_{\alpha*}, \mu_\delta) \sim (1, 1) \text{ mas yr}^{-1}$. From the 11 members with good quality *Gaia* astrometry, we calculate the systemic proper motion of Pic II to be $\overline{\mu}_{\alpha*} = 1.18 \pm 0.05 \text{ mas yr}^{-1}$ and $\overline{\mu}_\delta = 1.16 \pm 0.05 \text{ mas yr}^{-1}$ with the likelihood in Pace & Li (2019). Our measurement agrees with literature *Gaia* DR3 proper motion measurements (McConnachie & Venn 2020; Pace et al. 2022; Battaglia et al. 2022). We note that one member¹² is just outside our selection for good quality astrometry (`astrometric_excess_noise_sig=2.2`). While this star is excluded for our default measurement, including or excluding this star does not affect our systemic proper motion results.

4. DISCUSSION

4.1. The Nature of Pic II

Based on its size and luminosity, Pic II was considered an UFD galaxy candidate in the discovery analysis

¹¹ 10286300071017 does not have a IMACS CaT measurement due to low signal-to-noise nor a CaHK $[\text{Fe}/\text{H}]$ measurement due to the lack of i-band photometry. However, when g-r color is used in place of g-i color for the CaHK color-color diagram (i.e., in the lower-right hand panel of Figure 1), 10286300071017 clusters with the other Pic II members and is consistent with the Pic II metallicity.

¹² Gaia DR3 `source_id=5480248011928003968`

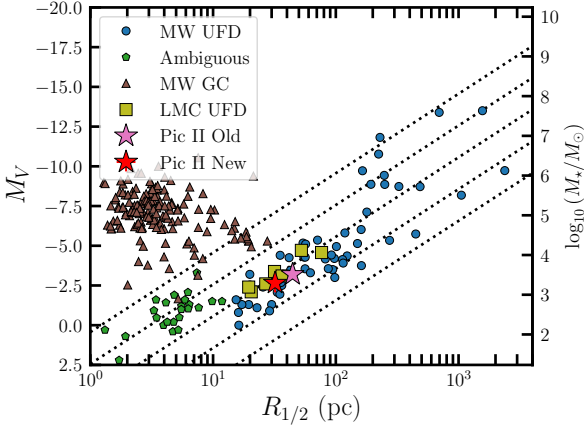


FIG. 3.— Size ($R_{1/2}$) versus absolute magnitude (M_V) comparison for MW satellites including dwarf galaxies, globular clusters, and ambiguous systems. We highlight LMC UFDs and the new and old Pic II measurements. Contours of constant surface brightness are indicated with dotted lines at 24, 26, 28, 30, 32 mag arcsec $^{-2}$.

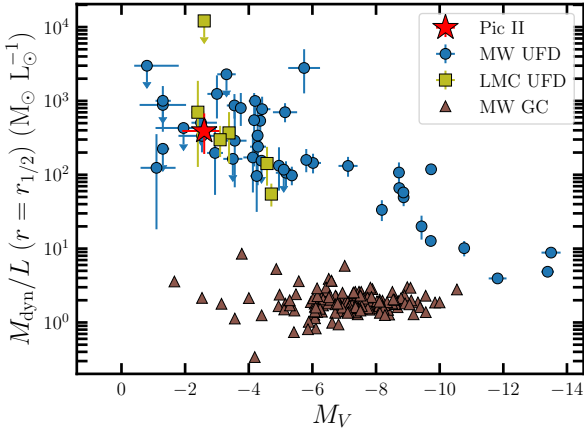


FIG. 4.— Absolute V-band magnitude vs dynamical mass-to-light ratio comparing Pic II (red star) to MW (blue circle) and LMC (gold squares) UFDs. The large mass-to-light ratio of Pic II is similar to other UFDs and Pic II is a dark matter-dominated dwarf galaxy.

(Drlica-Wagner et al. 2016). Following the definition of a galaxy from Willman & Strader (2012, i.e., the presence of a dark matter halo), our spectroscopic follow-up of Pic II and measurement of the large dynamical mass-to-light ratio (~ 700) confirms the dwarf galaxy classification. While a dynamical classification is the most straightforward, as the resolved dispersion is dependent on the membership and velocity of 2 stars in the 13 star member sample, it is worth exploring the other classification criteria.

A metallicity spread is indirect evidence for a presence of a dark matter halo massive enough to retain supernova ejecta to enable self-enrichment of a galaxy. The metallicity dispersion is not resolved with either CaT or CaHK [Fe/H] and this classification method is inconclusive for Pic II. The mean metallicity of Pic II is more metal-poor ($\overline{[Fe/H]} \sim -3$) than any intact MW globular

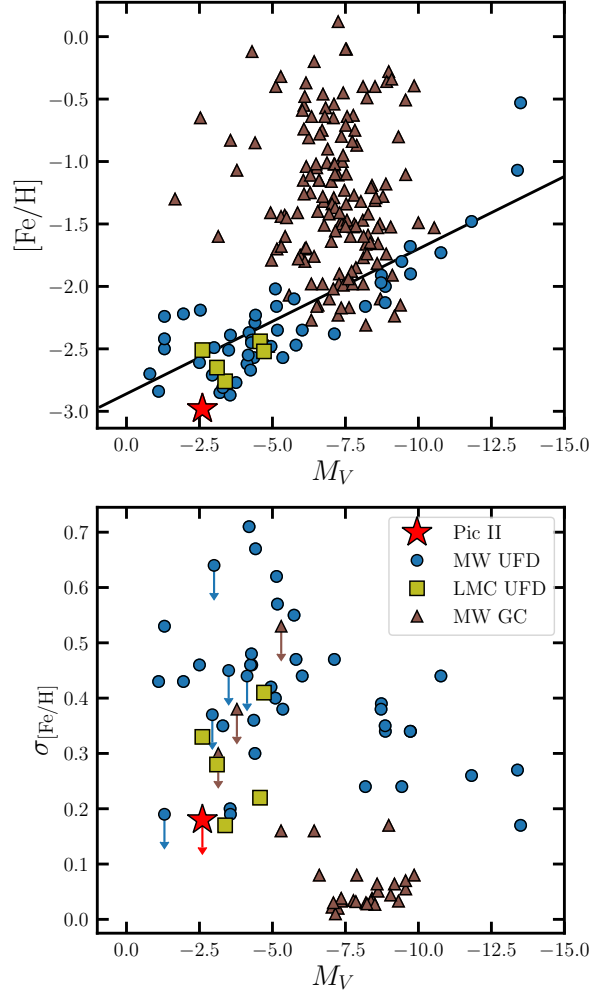


FIG. 5.— Absolute V-band magnitude vs metallicity ([Fe/H], top panel) or metallicity dispersion ($\sigma_{[Fe/H]}$, bottom panel) comparing Pic II (red star) to MW (blue circle) and LMC (gold squares) UFDs and MW globular clusters (brown triangle). The black line is the stellar mass-stellar metallicity relation (Kirby et al. 2013b; Simon 2019). Pic II is notably one of the most metal-poor UFD known.

cluster (Harris 1996) and is well below the globular cluster metallicity floor at $[Fe/H] \sim -2.5$ (e.g., Beasley et al. 2019). While there are some globular clusters stellar streams below the metallicity floor (e.g., Phoenix and C-19; Wan et al. 2020; Martin et al. 2022) as well as a M31 globular cluster (Larsen et al. 2020), the MW lacks any intact systems below this value. The updated size of Pic II ($r_{1/2} \sim 32$ pc) with DELVE DR3 photometry remains larger than the typical globular cluster (typically $r_{1/2} \lesssim 5$ pc but there are some GCs with $r_{1/2} \sim 5-20$ pc; Baumgardt & Hilker 2018) and it is located in the dwarf galaxy locus in the size-luminosity plane (see Figure 3).

Another defining characteristic of UFDs is their low neutron-capture element abundances from their inefficient star formation¹³ (e.g., Koch et al. 2008; Frebel &

¹³ Although there are some exceptions: Reticulum II, (Ji et al. 2016a; Roederer et al. 2016); Tucana III, (Hansen et al. 2017; Marshall et al. 2019), and Grus II (Hansen et al. 2020).

Norris 2015; Ji et al. 2019, 2020b). The neutron capture abundances for the brightest star in Pic II are consistent with this picture (Section 4.3). We only obtain upper limits for Ba, Eu, and Sr; the Sr and Ba upper limits exclude MW halo neutron capture values. Triangulum II and Grus I are examples of galaxies with unresolved or barely resolved velocity/metallicity dispersions, but whose low neutron-capture element content suggests they are (or once were) UFDs (Kirby et al. 2017; Venn et al. 2017; Ji et al. 2019). In contrast, all known globular clusters have moderately super-solar neutron-capture element abundances (e.g., Pritzl et al. 2005).

Lastly, we compare the properties of Pic II with the MW and LMC UFD population. In general, Pic II has properties similar to the bulk MW+LMC UFD population. As we show in the next section, Pic II is highly likely to be associated with the LMC and should be considered part of the LMC population for LMC and MW UFD comparisons (§ 4.2). Figure 3 compares the size and luminosity of the MW satellites and includes both UFDs and MW GCs. We note that at fixed M_V , the LMC UFDs are smaller on average than MW UFDs but there may be selection effects as the LMC and many of its satellites are at lower Galactic latitude with higher stellar background. In a more detailed statistical analysis Richstein et al. (2024) did not find any differences between the LMC and MW in the size-luminosity plane. Figure 4 shows the absolute V-band magnitude versus the dynamical mass-to-light ratio. Pic II follows the trend that lower luminosity UFDs have larger dynamical mass-to-light ratios.

Figure 5 shows the absolute V-band magnitude versus the metallicity and metallicity dispersion. Pic II is among the most metal-poor UFD known and is roughly 0.12 dex more metal-poor than Eridanus IV (Heiger et al. 2024), the previous most metal-poor UFD from spectroscopic measurements¹⁴. Interestingly, the LMC UFDs may be more metal-poor with smaller metallicity dispersions compared to MW UFDs with the caveats that there are a smaller number of LMC UFDs and the metallicity measurements come from an inhomogeneous sample. This may be due to lower star formation efficiencies of the LMC UFDs relative to the MW UFDs driven by their different environments. Our metallicity distribution measurements do not resolve a metallicity dispersion for Pic II.

We note that most dwarf galaxies contain RR Lyrae stars (e.g., Martínez-Vázquez 2023; Tau et al. 2024) and we present an unsuccessful RRL search in Appendix A. We list the literature references for Figures 3–5 in Appendix B.

In summary, based on its size, low metallicity, mass-to-light ratio, and chemical abundances, we conclude Pic II is an UFD and has properties similar to the UFD population.

4.2. Orbit and Connection to the Magellanic Clouds

With a distance of ~ 12 kpc from the LMC, Drlica-Wagner et al. (2016) suggested that Pic II was likely accreted with the LMC and gravitationally bound to the

LMC. With the 3D motions measured in this work, we compute the relative 3D velocity between the LMC and Pic II to be $166.0^{+14.9}_{-15.8}$ km s $^{-1}$ and an association is possible given the low relative velocity. Jethwa et al. (2016) built dynamical models to predict the phase space distribution of LMC and SMC UFD satellites. These models predict that Pic II will have a Galactic standard of rest line-of-sight velocity of $15 \text{ km s}^{-1} < v_{\text{gsr}} < 175 \text{ km s}^{-1}$ and Pic II measured value $v_{\text{gsr}} \sim 105 \text{ km s}^{-1}$ is in the middle of this distribution.

To verify a potential association, we compute the orbit of Pic II in a combined MW and LMC potential. We follow the methods of Erkal & Belokurov (2020) which treats the MW and LMC as individual particles that source their respective potentials and are able to move in response to each other. This technique accounts for the MW reflex motion with respect to the infall of the LMC (Gómez et al. 2015) and it includes the effect of dynamical friction of the MW on the LMC calculated with the prescription in Jethwa et al. (2016). For the MW potential, we use the McMillan (2017) potential, which includes an Navarro, Frenk, and White (NFW) halo (Navarro et al. 1996), a stellar bulge, and four disks (thin, thick, HI, and H2). To account for uncertainties in the MW potential, we sample over the posterior chains from the McMillan (2017) analysis. For the LMC potential, we use a Hernquist profile with a total mass of $1.38 \pm 0.255 \times 10^{11} M_\odot$ (from Erkal et al. 2019) and a scale radius chosen to match the enclosed mass of $1.7 \times 10^{10} M_\odot$ at 8.7 kpc from van der Marel & Kallivayalil (2014). In addition to Monte Carlo sampling over the LMC mass measurement, we sample over the observed phase space uncertainties including the radial velocity (van der Marel et al. 2002), the proper motion (Kallivayalil et al. 2013), and the distance (Pietrzyński et al. 2019). The orbit of Pic II is rewound for 5 Gyr or until the LMC passes its apocenter in the MW and LMC potential. For more details see Erkal & Belokurov (2020).

We use our new Pic II phase space measurements (Table 1 and Section 3) sampled over the observational uncertainties to compute the orbit of Pic II in the presence of the MW and LMC. In Figure 6, we show example orbits of Pic II and LMC UFDs with respect to the LMC and MW in both lookback time and spatial location. In this realization, the considered UFDs are gravitationally bound to the LMC, so their distances relative to the LMC are periodic. They also move away from MW as a group over time in galactocentric coordinates. Since we do not account for the evolution of the MW or the LMC potentials, we compute the pericenter and apocenter here at their global minimum and maximum with respect to the MW or LMC. We find the pericenter and apocenter of Pic II are ~ 39 kpc and ~ 219 kpc with respect to the MW and are ~ 8 kpc and ~ 30 kpc with respect to the LMC. D’Souza & Bell (2022) find that the most recent pericenter and apocenter can be reliably determined during backwards integration but previous pericenters or apocenters are more unreliable.

We estimate the probability of Pic II being an LMC satellite by computing its energy relative to the LMC 5 Gyr ago (at the end of integration) following Erkal & Belokurov (2020) to determine whether they were en-

¹⁴ We note that Canes Venatici II and Hydra II have photometric CaHK metallicities that are more metal-poor or around the same metallicity as Pic II (Fu et al. 2023).

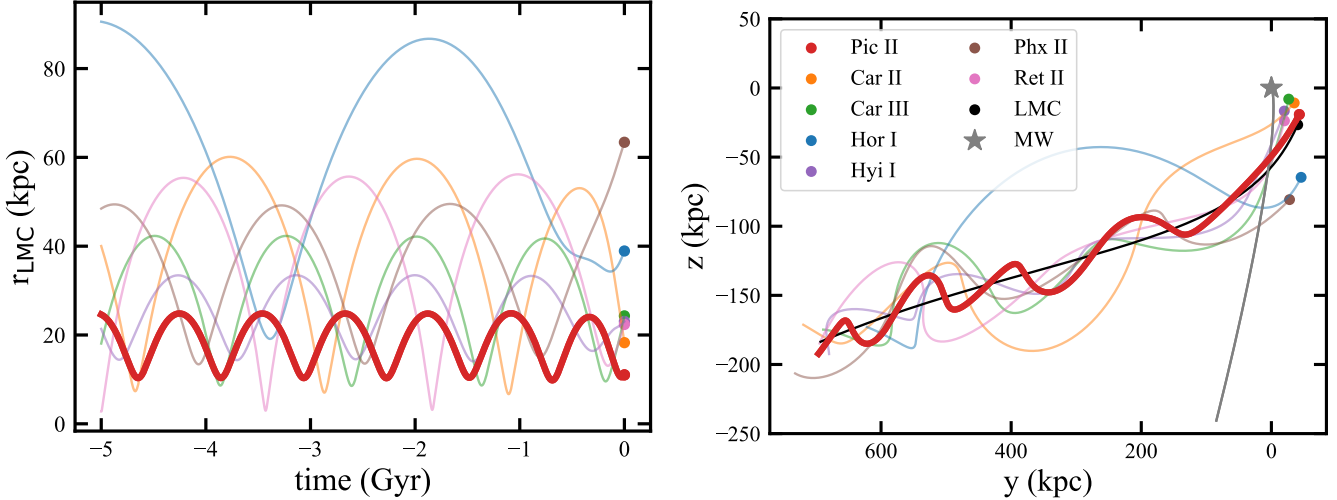


FIG. 6.— Example orbits of Pic II and other LMC associated UFDs relative to the LMC and MW. **Left:** Lookback time versus relative distance to the LMC. Periodicity of plotted distances shows that the considered UFDs are gravitationally bound to the LMC in a given realization. **Right:** Galactocentric coordinates (y vs z) relative to the current MW center. As the UFDs shown in this example are bound to the LMC, they move away from MW as a group over time.

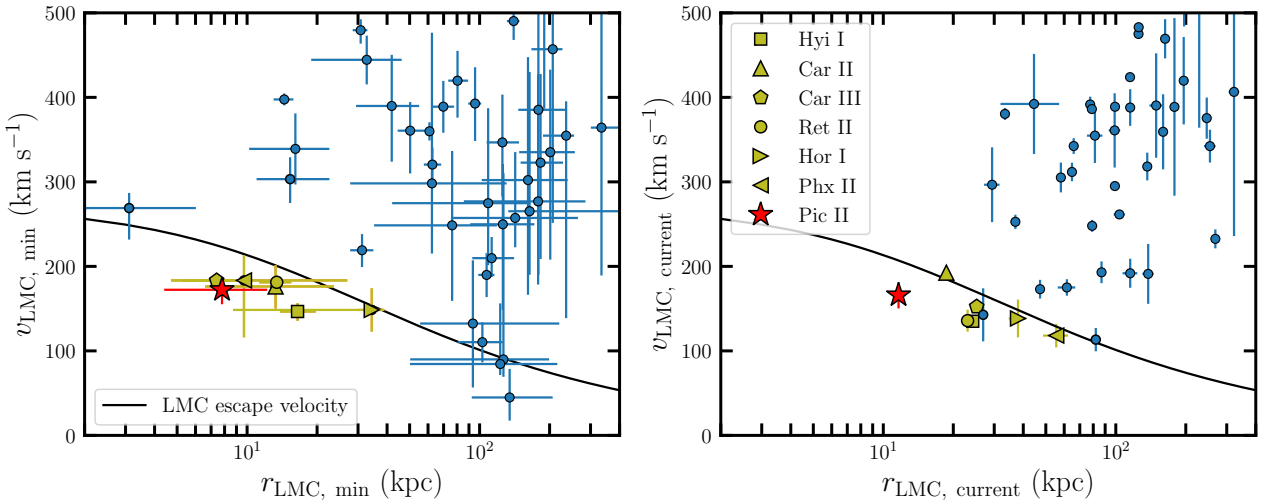


FIG. 7.— Distance and velocity relative to the LMC at each UFD’s previous closest approach to the LMC (left) and current distance and velocity relative to the LMC (right). Both at closest approach and present moment, Pic II (red star) and other confirmed LMC UFDs (gold symbols) are under or very close to the LMC escape velocity curve, which is further evidence of their association with the LMC. The MW UFD (blue circles) data is from Pace et al. (2022). The black line is the LMC escape velocity curve with $M_{\text{LMC}} = 1.38 \times 10^{11} M_{\odot}$.

ergetically bound. If the LMC reaches the apocenter before 5 Gyr, we stop the rewinding and compute the energy at that time. With this definition, we compute that Pic II has a 91% association probability with the LMC¹⁵. We show this visually in Figure 7, where we show the minimum distance between Pic II and LMC compared to the relative velocity between Pic II and the LMC along with the current values. We note that Correa Magnus & Vasiliev (2022) computed orbits of Pic II in a LMC and MW potential but varied the line-of-sight

velocity between -200 to 800 km s $^{-1}$ and found that at $v_{\text{hel}} \sim 330$ km s $^{-1}$ the probability of LMC association is near 100% (in particular the range of 100 to 500 km s $^{-1}$ has high probability for LMC association).

Pic II is the seventh LMC UFD to be confirmed with full phase space measurements and orbit modeling. The spatial distribution of the LMC UFDs is asymmetric and there are more LMC UFDs in the leading orbit of the LMC (Car II, Car III, Hyi I, Pic II, and Ret II) than trailing the orbit (Hor I and Phe II). This spatial anisotropy is similar to M31 (e.g., McConnachie & Irwin 2006; Savino et al. 2022), where there are more satellites on the MW side of the satellite system compared to the far side. With the LMC system there are fewer confirmed

¹⁵ Patel et al. (2020) present an alternative LMC probability that is determined on whether the satellite was within the escape velocity of the LMC at its most recent approach to the LMC and we find similar results with this definition.

UFDs overall and the system is being tidally heated by the MW. The satellite sensitivity is lower for more distant systems and the coverage for satellite searches is lower on the southern side of the LMC and this asymmetry may be due to selection effects. Of the known UFD candidates without spectroscopy, DELVE 2 (Cerny et al. 2021a) is a candidate member of the LMC system based on its spatial location and proper motion (Cerny et al. 2021a; Correa Magnus & Vasiliev 2022; Vasiliev 2024) and it is located on the far side of the LMC.

In Figure 8, we show the orbital pericenter versus average density within the half-light radius for Pic II, MW UFDs, and LMC UFDs. Strong tidal disruption is expected when the average UFD density is less than twice the average MW or LMC density at its pericenter. Pic II is unlikely to be strongly stripped by the MW based on the Jacobii radius approximation. The right-hand panel of Figure 8 repeats the same exercise but with respect to the LMC instead of the MW. The overall tidal influence the LMC exerts on its UFDs is smaller than the MW exerts on its UFDs due to its roughly order of magnitude smaller halo mass. The orbital pericenters with respect to the LMC of the LMC UFDs are generally smaller than the MW UFDs with respect to the MW and vary between $\approx 6 - 30$ kpc here. While Pic II has a smaller pericenter (~ 8 kpc) with respect to the LMC compared to the MW, its tidal radius is still much greater than its half-light radius and strong tidal stripping is not expected.

To more quantitatively estimate the Pic II tidal radius¹⁶ with respect to the LMC, we first compute the tidal radius with $r_t = r_{\text{peri}} (m_{\text{UFD}}/2M_{\text{host}})^{1/3}$ which assumes the host has a flat rotation curve and the satellite is on a circular orbit (King 1962). For the tidal radius computations, we assume that the mass distribution of Pic II follows an NFW profile with several different scale radius values (specifically $r_s = 40, 100, 200$ pc) and set the scale density based on matching the $M_{1/2}$ dynamical mass. We assume that the LMC mass follows a Hernquist profile as above. We find $r_t = 330, 450, 590$ pc for $r_s = 40, 100, 200$ pc. The smallest r_s value is set by the size of Pic II (~ 32 pc). These tidal radii are more than 10 times larger than the half-light radius.

To account for the non-circular motion and extended mass profiles, we also compute the tidal radius using $r_t = \left[(G m_{\text{UFD}})/(\Omega^2 - \frac{d^2\phi_{\text{host}}}{dR^2}) \right]^{1/3}$, where Ω is the angular speed and ϕ is the LMC gravitational potential (King 1962). Here we find smaller tidal radii with the same scale radii values, $r_t = 190, 270, 340$ pc and the smallest value is approximately 5 times larger than the half-light radius. We note that in both the FIRE (Shipp et al. 2023) and Auriga (Riley et al. 2024; Shipp et al. 2024) simulations nearly all dwarf galaxy satellites in MW-like galaxies are undergoing tidal stripping and contain tidal tails but these are commonly below current detection limits (Shipp et al. 2023). However, we note that some disruption in simulations may be numerical (van den Bosch et al. 2018). We note that the actual tidal radius should also account for the MW and SMC but both will have a smaller impact relative to the LMC.

¹⁶ See van den Bosch et al. (2018) for an overview of the different tidal radius definitions.

4.3. Detailed abundances of an extremely metal-poor star

With $[\text{Fe}/\text{H}] = -3.3$, PicII-1 is one of the most Fe-poor stars known in any UFD. As such, the abundances of this star are closely connected to the nucleosynthetic yields of the first metal-free (Pop III) stars (e.g., Ji et al. 2015). Still, most of its abundance ratios are quite similar to other metal-poor stars found in UFDs: the $[\alpha/\text{Fe}]$ ratios are enhanced; most elements up to the iron peak are similar to halo stars at $[\text{Fe}/\text{H}] \sim -3$; and the neutron-capture element abundances are low compared to typical halo stars. The abundances of PicII-1 are similar to one of the most metal-poor stars in the Coma Berenices UFD (ComBer-S2 from Frebel et al. 2010). ComBer-S2 is enhanced in Mg and Sc, deficient in Mn, is not Carbon enhanced, and lacks neutron-capture elements (Frebel et al. 2010). In Figure 9, we compare the $[\text{C}/\text{Fe}]$, $[\text{Mg}/\text{Fe}]$, $[\text{Sc}/\text{Fe}]$, and $[\text{Ba}/\text{Fe}]$ abundances to a representative MW halo sample and abundance measurements from other UFDs. The low neutron-capture element abundances lend additional confidence that Pic II is a dwarf galaxy and not a star cluster (see Section 4.1) (Ji et al. 2019).

Carbon-enhanced metal-poor stars are thought to be especially related to Pop III stars (e.g., Frebel & Norris 2015). About 40% of halo stars with $[\text{Fe}/\text{H}] < -3$ have $[\text{C}/\text{Fe}] > 0.7$ (Placco et al. 2014; Arentsen et al. 2022), but it is still debated whether a similar trend is found in dwarf galaxies like Sculptor (e.g., Salvadori et al. 2015; Chiti et al. 2018a) and Sagittarius (e.g., Limberg et al. 2023; Sestito et al. 2024). We measure this Pic II star to have $[\text{C}/\text{Fe}] = -0.36$, and corrections for internal mixing in red giant evolution (Placco et al. 2014) suggest a natal abundance $[\text{C}/\text{Fe}] \approx +0.37$. This star is thus clearly *not* significantly carbon-enhanced. Including this star, there are now 22 stars across 9 UFDs that have $[\text{Fe}/\text{H}] < -3$ and carbon measurements: 3 in Segue1, (Frebel et al. 2014); 2 in UMa II, (Frebel et al. 2010); 3 in Bootes I, (Norris et al. 2010; Gilmore et al. 2013; Frebel et al. 2016); 3 in Ret II; (Ji et al. 2016c; Roederer et al. 2016); 6 in Tuc II, (Ji et al. 2016d; Chiti et al. 2018b, 2023); 2 in Car II (Ji et al. 2020b); 1 in Car III (Ji et al. 2020b); and 1 in Tuc V (Hansen et al. 2024). 13 (8) of these 22 stars are carbon-enhanced with $[\text{C}/\text{Fe}] > 0.7 (> 1.0)$, which is higher than but consistent with the stellar halo fraction, as shown in Ji et al. (2020b). We note that every one of these UFDs other than Pic II has at least one carbon-enhanced star at $[\text{Fe}/\text{H}] < -3$, but with one star in Pic II it would be premature to conclude that Pic II does not contain any carbon-enhanced stars (e.g., Koch et al. 2008; Gilmore et al. 2013; Ishigaki et al. 2014; Ji et al. 2016d, 2019, 2020b; Chiti et al. 2023; Waller et al. 2023; Webber et al. 2023; Hansen et al. 2024).

The α -elements (magnesium, silicon, calcium, titanium) in this Pic II star have super-solar ratios, similar to stars in all UFDs other than Hor I. Nagasawa et al. (2018) found three stars in that system with $[\alpha/\text{Fe}] \approx 0$. As Hor I is very likely associated with the LMC (Koposov et al. 2015b), those authors hypothesized that the low α -element abundances could be an indication of association with the LMC, possibly due to an overall lower star formation efficiency for galaxies forming near the LMC instead of the MW. However, both Car II (Ji et al.

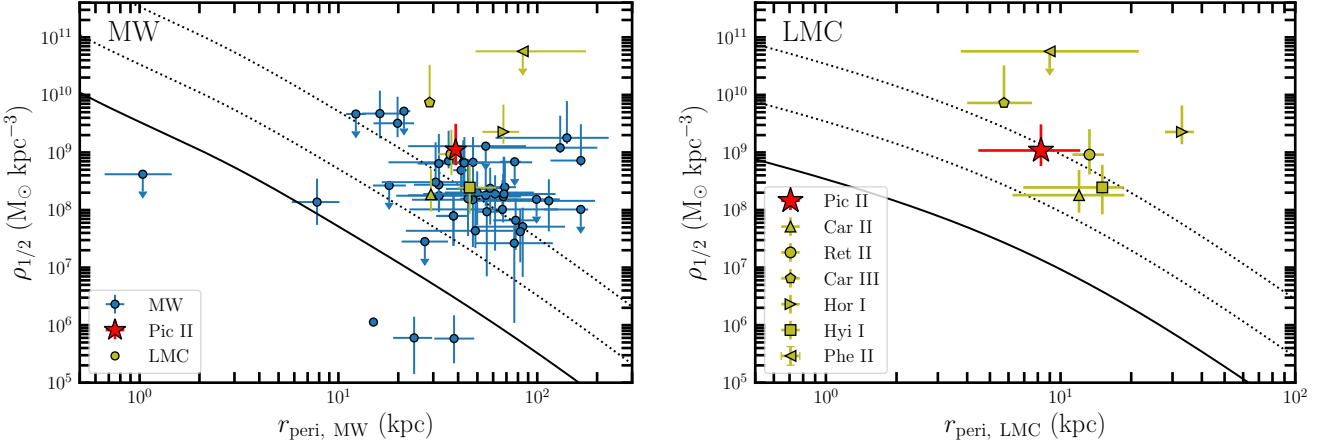


FIG. 8.— **Left:** Orbital pericenter with respect to the MW versus average density with the half-light radius for MW UFDs (blue points), LMC UFDs (gold points), and Pic II (red point). The MW and LMC measurements are primarily from Pace et al. (2022) but include newer literature measurements. The solid black line is the twice the average MW density and this line denotes where the tidal radius at pericenter will be smaller or larger than the half-light radius. The dotted lines are 10 and 100 times this value. **Right:** Orbital pericenter with respect to the LMC versus average density with the half-light radius for Pic II and other LMC UFDs. The solid line is twice the average LMC density and the dotted lines are 10 and 100 times this value.

2020b) and Ret II (Ji et al. 2016c; Roederer et al. 2016), two other LMC UFDs, do not show this trend. Pic II provides additional evidence against that hypothesis, as it is also clearly associated with the LMC but contains a star with enhanced $[\alpha/\text{Fe}]$ ratios. However, this Pic II star has $[\text{Fe}/\text{H}] = -3.3$, significantly lower than the $[\text{Fe}/\text{H}] \sim -2.6$ stars studied so far in Hor I. This low- $[\text{Fe}/\text{H}]$ star does not probe the late-time chemical evolution of the system, and so cannot really test the hypothesis that star formation efficiencies are different for LMC satellites. Unfortunately, we currently have no α -element constraints in Pic II stars of higher $[\text{Fe}/\text{H}]$.

Ratios of different α -elements provide some constraint on the progenitor mass of a core-collapse supernova (e.g., McWilliam et al. 2013; Carlin et al. 2018; Ji et al. 2020b). In particular, the yield of hydrostatically synthesized elements like Mg increases significantly with progenitor mass, while explosively synthesized elements like Ca are less affected by progenitor mass. The detailed relation between $[\text{Mg}/\text{Ca}]$ and progenitor mass is not straightforward, as Ca yields are affected by the SN explosion, but higher $[\text{Mg}/\text{Ca}]$ ratios correspond to higher progenitor masses on average (e.g., Heger & Woosley 2010). We measure $[\text{Mg}/\text{Ca}] = 0.51 \pm 0.14$ in this star, a high ratio that suggests this Fe-poor star is predominantly (or perhaps only) enriched by relatively massive core-collapse supernovae.

Ji et al. (2020b) explored the evolution of $[\text{Mg}/\text{Ca}]$ versus $[\text{Fe}/\text{H}]$ for the UFD population and while most UFDs do not show a trend with $[\text{Fe}/\text{H}]$, two LMC satellites (Car II and Ret II), show a declining trend with increasing $[\text{Fe}/\text{H}]$. The lowest metallicity star in Car III also has high $[\text{Mg}/\text{Ca}]$ but there are only two stars in Car III with chemical abundance measurements. This trend and its difference from other non-LMC UFDs could be evidence for environmental effects in the chemical evolution of a UFD (see Section 4.3.3 of Ji et al. 2020b). However, Hansen et al. (2024) recently showed that Tu-

cana V, which does not appear to be associated with the LMC, also exhibits a similar $[\text{Mg}/\text{Ca}]$ trend as the Magellanic satellites identified by Ji et al. (2020b). The star formation histories of LMC UFDs suggest they formed later (Sacchi et al. 2021; Simon et al. 2023; Durbin et al. 2025). While we cannot determine how $[\text{Mg}/\text{Ca}]$ evolves with $[\text{Fe}/\text{H}]$ in Pic II, the high value of $[\text{Mg}/\text{Ca}] = 0.51$ at $[\text{Fe}/\text{H}] = -3.3$ suggests Pic II may follow the trend observed in other LMC UFDs.

The main other element of note is scandium. We measured $[\text{Sc}/\text{Fe}] = 0.59 \pm 0.18$ from 7 different lines, an unusually high value compared to other UFDs and halo stars at similar $[\text{Fe}/\text{H}]$. We fit synthetic spectra including hyperfine splitting for all Sc lines, the line-to-line abundance scatter is low, and variations due to stellar parameters are included in the uncertainty. We also verify that our analysis method reproduces the Sc abundance of several other UFD and standard halo stars to within 0.1 dex. The somewhat high Sc abundance in this star is thus real and significant, at least in 1D LTE (3D and NLTE effects for Sc II have not been investigated in metal-poor red giant stars, Bergemann & Nordlander 2014). The interpretation of high Sc is somewhat unclear, as standard models of core-collapse supernovae tend to under-produce Sc (see discussion in Nomoto et al. 2013; Curtis et al. 2019). Two ways of increasing Sc production include the νp -process (Fröhlich et al. 2006) or high-energy hypernova (Nomoto et al. 2006), but the other elements available in our Pic II star do not constrain these processes. We note that Zn tends to be produced with Sc in these models, but our spectrum provides only a weak 3σ (5σ) limit of $[\text{Zn}/\text{Fe}] < +1.03$ (+1.30). Overall, it seems that there could be substantial $[\text{Sc}/\text{Fe}]$ variation across different UFDs (e.g., Ji et al. 2020b; Chiti et al. 2023), which may point to interesting variations in the first supernova explosions.

4.4. Astrophysical J-factor and D-factor

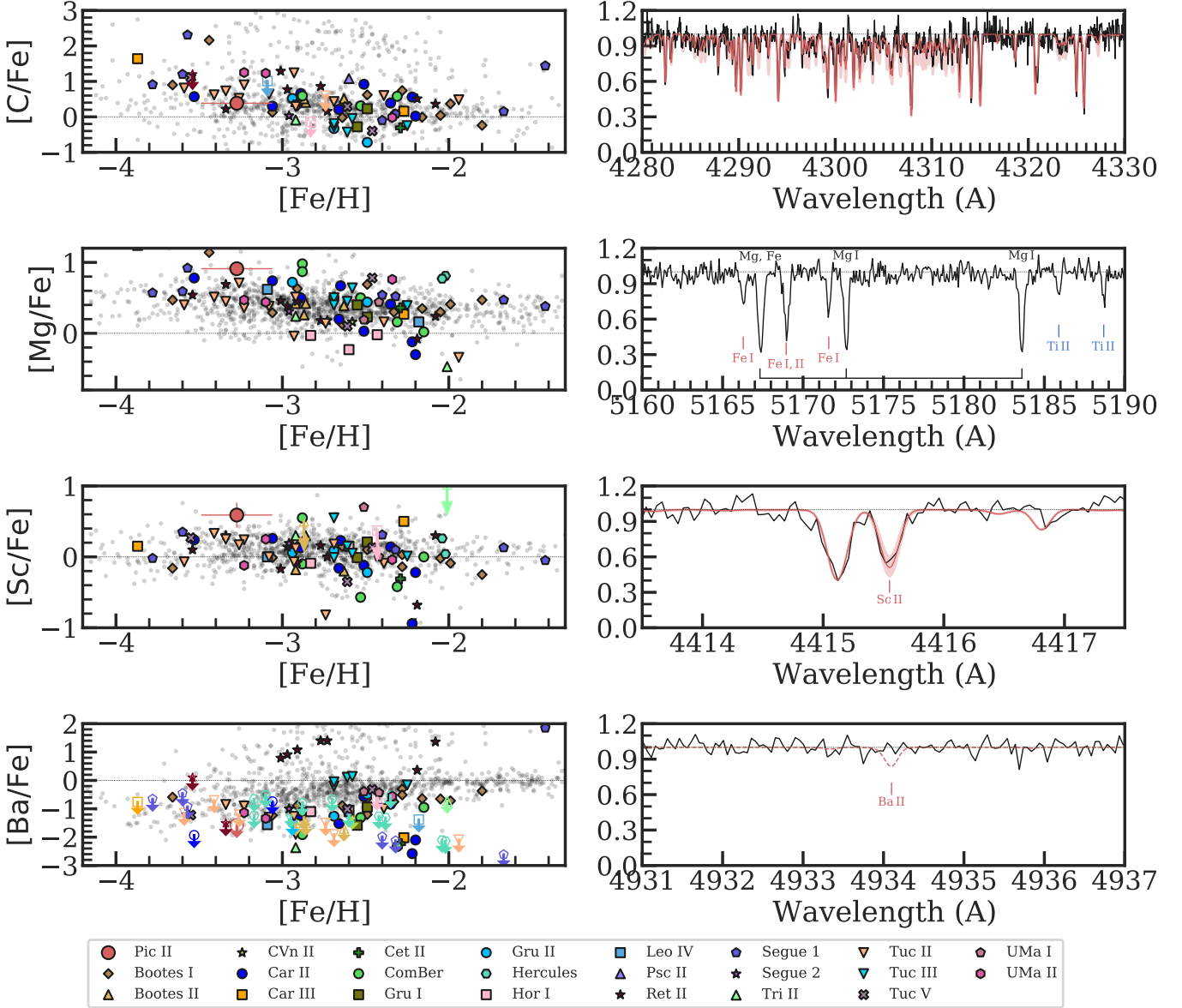


FIG. 9.— **Left:** Detailed abundances of PicII-1, the brightest Pic II star (large red circle) compared to halo stars (grey points, from Abohalima & Frebel 2018) and other UFD stars (colored points). **Right:** Normalized MIKE spectra of the target star around the CH bands, Mg b triplet, a Sc line, and a Ba line. For CH and Sc, the synthesized fit shown as a red line, with 2σ abundance errors shaded. For Ba, a dashed red line shows the 5σ upper limit. The literature references are listed in Appendix B

The MW UFDs are among the most promising targets for searches of the products of dark matter annihilation or decay as they are nearby, highly dark matter-dominated, and nearly background free (e.g., Ackermann et al. 2015; Geringer-Sameth et al. 2015a; McDaniel et al. 2024; Circiello et al. 2025). While some individual UFDs are excellent targets on their own, new UFDs are also useful in stacked joint analyses to boost any signal or exclusion limits (e.g., Ackermann et al. 2011; Geringer-Sameth & Koushiappas 2011) and we analyze Pic II here for future dark matter indirect detection studies.

The astrophysical component of the annihilation or decay flux is known as the J-factor or D-factor, respectively. The J-factor is the integral of the dark matter density

squared over the line-of-sight: $J(\theta) = \int \rho_{\text{DM}}^2 d\Omega dl$. The D-factor is the linear analog: $D(\theta) = \int \rho_{\text{DM}} d\Omega dl$. Here, ρ_{DM} is the dark matter density profile and the integral is performed over the solid angle, $\Delta\Omega$, and along the line-of-sight, l . The standard procedure in MW dwarf spheroidal galaxies to determine ρ_{DM} is to fit line-of-sight stellar kinematic data with dynamical mass models computed from the spherical Jeans equations¹⁷ (e.g., Strigari et al. 2008; Bonnivard et al. 2015; Pace & Strigari 2019).

We follow Pace & Strigari (2019) for our J-factor analysis and briefly summarize the procedure. For the spher-

¹⁷ Although other dynamical mass models have been used (e.g., Hayashi et al. 2016; Evans et al. 2016).

ical Jeans modeling, we assume the stellar density profile follows a Plummer distribution (Plummer 1911), the dark matter profile is an NFW halo (Navarro et al. 1996), and the stellar anisotropy is constant with radius. We account for observational errors in the structural parameters and compare the line-of-sight velocity dispersion from Jeans equations solutions to observed stellar kinematics with an unbinned likelihood (Martinez et al. 2011; Geringer-Sameth et al. 2015b). For the J- and D-factor calculation, the extent of the DM halo is required. We use the tidal radius computed at the orbital pericenter with respect to the LMC as it is smaller than the MW tidal radius. We fix $r_t = 0.4$ kpc (or $r_t = 0^\circ.51$) following the discussion in Section 4.2. We note that few J-factor measurements in the literature have computed the tidal radius at the orbital pericenter as many measurements predate *Gaia* proper motion measurements.

We measure the J-factor to be: $\log_{10} (J/\text{GeV}^2\text{cm}^{-5}) = 18.15^{+0.54}_{-0.53}$, 18.33 ± 0.53 , 18.48 ± 0.55 for solid angles of $\theta = 0^\circ.1, 0^\circ.2, 0^\circ.5$ (the J-factor does not increase beyond the tidal radius of $0^\circ.51$). Similarly, the D-factor we measure is: $\log_{10} (D/\text{GeV}^2\text{cm}^{-5}) = 17.02 \pm 0.28$, $17.45^{+0.30}_{-0.31}$, $17.86^{+0.33}_{-0.39}$ for solid angles of $\theta = 0^\circ.1, 0^\circ.2, 0^\circ.5$ ($r_t = 0.4$ kpc). The J-factor we measure matches the dynamical J-factor scaling relations introduced in Pace & Strigari (2019), however, it does not match the predictions of the luminosity based scaling relations (the prediction is $\log_{10} (J(0.5^\circ)) = 18.9$). If the tidal radius is decreased to $r_t = 0.3$ kpc (or $r_t = 0^\circ.38$), the J-factor and D-factor at smaller angles only slightly decrease whereas the maximum angle decreases to $\log_{10} (J/\text{GeV}^2\text{cm}^{-5}) = 18.42^{+0.53}_{-0.54}$ and $\log_{10} (D/\text{GeV cm}^{-2}) = 17.66^{+0.31}_{-0.34}$ for a solid angle of $\theta = 0^\circ.38$. The impact and decrease in the J-factor will be larger for smaller values of the tidal radius. We note that the D-factor is impacted more than the J-factor with smaller tidal radii. Pic II is a good target for dark matter annihilation searches as the J-factor is fairly large (there are 15 MW dwarf galaxies larger in Figure 11 in Heiger et al. 2024) and it will be a useful addition in stacked analysis.

5. SUMMARY

We have presented the first stellar spectroscopy of the UFD candidate Pic II. Our results are summarized as follows:

- Using DELVE DR3 and the `ugali` package, we have updated the morphological parameters with data approximately 1 magnitude deeper than the discovery analysis. Our updated results find Pic II to be slightly smaller ($R_{1/2} \sim 32$ pc) and fainter ($M_V \sim -2.6$) than previous measurements.
- We obtained 4 epochs of Magellan/IMACS medium resolution stellar spectroscopy and identified 13 radial velocity members. We determined the systemic heliocentric velocity of Pic II to be $v_{\text{hel}} = 326.9 \pm 1.1$ km s $^{-1}$ and resolve the velocity dispersion to be $\sigma_v = 3.5^{+1.1}_{-0.9}$ km s $^{-1}$.
- We measured both spectroscopic and photometric stellar metallicities ([Fe/H]) with Calcium Triplet equivalent widths and CaHK photometry and find

good agreement. From spectroscopic [Fe/H], we found $[\text{Fe}/\text{H}] = -2.99 \pm 0.06$ for Pic II but are not able to resolve the metallicity dispersion ($\sigma_{[\text{Fe}/\text{H}]} < 0.18$; 95% credible level).

- We determined detailed chemical abundances of 13 elements with a high resolution spectrum of the brightest Pic II star with Magellan/MIKE. Notably, the star is extremely metal-poor ($[\text{Fe}/\text{H}] = -3.3$), enhanced in α elements, and deficient in neutron-capture elements, similar to the abundances in other UFDs. However, this star has an unusually high [Sc/Fe] ratio.
- The dynamical mass-to-light ratio (~ 760), size, and low neutron-capture elements confirm that Pic II is a dark matter-dominated UFD galaxy.
- We computed the orbit of Pic II in a combined MW and LMC potential and found that Pic II is bound to the LMC in 91% of modeled orbits and likely entered the MW system with the LMC. The orbital parameters with respect to the LMC are $r_{\text{peri}, \text{LMC}} = 7.8^{+4.4}_{-3.4}$ kpc and $r_{\text{apo}, \text{LMC}} = 29.9^{+9.7}_{-6.0}$ kpc. Pic II is the 7th UFD confirmed to be associated with the LMC based on its measured phase space and orbital analysis. Pic II is likely still bound to the LMC today.
- We computed the dark matter properties of Pic II in the context of dark matter indirect detection studies and measured the predicted annihilation and decay flux. Pic II has a fairly typical J-factor of $\log_{10} J(0.5^\circ) = 18.50 \pm 0.55$ and will be a useful target in future searches.

The Legacy Survey of Space and Time (Ivezic et al. 2019) at the upcoming Vera C. Rubin Observatory will find many more UFDs and potentially more LMC associated systems (e.g., Tsiane et al. 2025). Identifying LMC associated UFDs will enable the study of UFDs that formed in a lower density environment. Stellar spectroscopic follow-up of UFD candidates is key to classify and confirm these systems and to determine their kinematics, orbital properties, metallicity distributions, and dark matter properties. The next generation of instruments (e.g., VLT/MOONS¹⁸, VIA¹⁹, Subaru Prime Focus Spectrograph²⁰), ongoing and upcoming surveys (e.g., DESI, 4MOST), and the next generation of 30 m-class telescopes will be key to characterize the distant UFDs that will be found with Legacy Survey of Space and Time, Euclid, and the Nancy Grace Roman Space Telescope.

ACKNOWLEDGMENTS

We thank Andrew Casey and Anna Frebel for co-developing the latest version of SMH. We thank Chris Garling for useful discussions. APJ was supported

¹⁸ <https://vltnmoons.org/>

¹⁹ <https://via-project.org/>

²⁰ <https://pfs.ipmu.jp>

by NASA through Hubble Fellowship grant HST-HF2-51393.001 awarded by the Space Telescope Science Institute, which is operated by the Association of Universities for Research in Astronomy, Inc., for NASA, under contract NAS5-26555. W.C. gratefully acknowledges support from a Gruber Science Fellowship at Yale University. This material is based upon work supported by the National Science Foundation Graduate Research Fellowship Program under Grant No. DGE2139841. Any opinions, findings, and conclusions or recommendations expressed in this material are those of the author(s) and do not necessarily reflect the views of the National Science Foundation. AC is supported by a Brinson Prize Fellowship at UChicago/KICP.

T.S.Li and G.E.M. acknowledges financial support from Natural Sciences and Engineering Research Council of Canada (NSERC) through grant RGPIN-2022-04794. G.E.M. acknowledges support from an Arts & Science Postdoctoral Fellowship at the University of Toronto. The Dunlap Institute is funded through an endowment established by the David Dunlap family and the University of Toronto. The work of V.M.P. is supported by NOIRLab, which is managed by the Association of Universities for Research in Astronomy (AURA) under a cooperative agreement with the U.S. National Science Foundation. DJS acknowledges support from NSF grant AST-2205863.

This research has made use of the SIMBAD database, operated at CDS, Strasbourg, France (Wenger et al. 2000), NASA’s Astrophysics Data System Bibliographic Services, and the arXiv preprint server.

The DECam Local Volume Exploration Survey (DELVE; NOAO Proposal ID 2019A-0305, PI: Drlica-Wagner) is partially supported by Fermilab LDRD project L2019-011 and the NASA Fermi Guest Investigator Program Cycle 9 No. 91201. The DELVE project is partially supported by the National Science Foundation under Grant No. AST-2108168 and AST-2307126.

This work has made use of data from the European Space Agency (ESA) mission *Gaia* (<https://www.cosmos.esa.int/gaia>), processed by the *Gaia* Data Processing and Analysis Consortium (DPAC, <https://www.cosmos.esa.int/web/gaia/dpac/consortium>). Funding for the DPAC has been provided by national institutions, in particular the institutions participating in the *Gaia* Multilateral Agreement.

This project used public archival data from the Dark Energy Survey (DES). Funding for the DES Projects has been provided by the U.S. Department of Energy, the U.S. National Science Foundation, the Ministry of Science and Education of Spain, the Science and Technology FacilitiesCouncil of the United Kingdom, the Higher Education Funding Council for England, the National Center for Supercomputing Applications at the University of Illinois at Urbana-Champaign, the Kavli Institute of Cosmological Physics at the University of Chicago, the Center for Cosmology and Astro-Particle Physics at the Ohio State University, the Mitchell Institute for Fundamental Physics and Astronomy at Texas A&M University, Financiadora de Estudos e Projetos, Fundação Car-

los Chagas Filho de Amparo à Pesquisa do Estado do Rio de Janeiro, Conselho Nacional de Desenvolvimento Científico e Tecnológico and the Ministério da Ciência, Tecnologia e Inovação, the Deutsche Forschungsgemeinschaft, and the Collaborating Institutions in the Dark Energy Survey.

The Collaborating Institutions are Argonne National Laboratory, the University of California at Santa Cruz, the University of Cambridge, Centro de Investigaciones Energéticas, Medioambientales y Tecnológicas-Madrid, the University of Chicago, University College London, the DES-Brazil Consortium, the University of Edinburgh, the Eidgenössische Technische Hochschule (ETH) Zürich, Fermi National Accelerator Laboratory, the University of Illinois at Urbana-Champaign, the Institut de Ciències de l’Espai (IEEC/CSIC), the Institut de Física d’Altes Energies, Lawrence Berkeley National Laboratory, the Ludwig-Maximilians Universität München and the associated Excellence Cluster Universe, the University of Michigan, the National Optical Astronomy Observatory, the University of Nottingham, The Ohio State University, the OzDES Membership Consortium, the University of Pennsylvania, the University of Portsmouth, SLAC National Accelerator Laboratory, Stanford University, the University of Sussex, and Texas A&M University.

Based in part on observations at Cerro Tololo Inter-American Observatory, National Optical Astronomy Observatory, which is operated by the Association of Universities for Research in Astronomy (AURA) under a co-operative agreement with the National Science Foundation.

This paper includes data gathered with the 6.5 meter Magellan Telescopes located at Las Campanas Observatory, Chile.

Facilities: Magellan-Baade (IMACS, Dressler et al. 2006, 2011), Magellan-Clay (MIKE, Bernstein et al. 2003)

SOFTWARE

`astropy` (Astropy Collaboration et al. 2013, 2018), `matplotlib` (Hunter 2007), `NumPy` (Walt et al. 2011), `iPython` (Pérez & Granger 2007), `SciPy` (Virtanen et al. 2020) `corner.py` (Foreman-Mackey 2016), `emcee` (Foreman-Mackey et al. 2013), `gala` (Price-Whelan 2017), `galpy`²¹ (Bovy 2015), `CarPy` (Kelson 2003), `MOOG` (Sneden 1973; Sobeck et al. 2011) SMH (Casey 2014) `pandas` (pandas development team 2020), `seaborn` (Waskom et al. 2016), `pocoMC` (Karamanis et al. 2022a,b), NOIRLab IRAF (Tody 1986, 1993; Fitzpatrick et al. 2024)

DATA AVAILABILITY

DELVE DR3 photometry will be released in an upcoming data release (Drlica-Wagner in prep.) and the MAGIC photometry with be contained in the first public data release (Chiti et al. in prep). Our Magellan/IMACS member catalog is in Table 3 while the full catalog is in the following zenodo repository: <https://doi.org/10.5281/zenodo.15706700>.

²¹ <http://github.com/jobovy/galpy>

REFERENCES

- Abbott T. M. C., et al., 2021, ApJS, 255, 20
- Abohalima A., Frebel A., 2018, ApJS, 238, 36
- Ackermann M., et al., 2011, Phys. Rev. Lett., 107, 241302
- Ackermann M., et al., 2015, Physical Review Letters, 115, 231301
- Alonso-García J., et al., 2025, A&A, 695, A47
- Anbajagane D., et al., 2025, arXiv e-prints, p. arXiv:2502.17674
- Arentsen A., Placco V. M., Lee Y. S., Aguado D. S., Martin N. F., Starkenburg E., Yoon J., 2022, MNRAS, 515, 4082
- Asplund M., Grevesse N., Sauval A. J., Scott P., 2009, ARA&A, 47, 481
- Astropy Collaboration et al., 2013, A&A, 558, A33
- Astropy Collaboration et al., 2018, AJ, 156, 123
- Balbinot E., et al., 2013, ApJ, 767, 101
- Bandyopadhyay A., Ezzeddine R., Placco V. M., Frebel A., Aguado D. S., Roederer I. U., 2025, arXiv e-prints, p. arXiv:2505.04001
- Barbosa F. O., et al., 2025, arXiv e-prints, p. arXiv:2504.03593
- Battaglia G., Taibi S., Thomas G. F., Fritz T. K., 2022, A&A, 657, A54
- Baumgardt H., Hilker M., 2018, MNRAS, 478, 1520
- Baumgardt H., Vasiliev E., 2021, MNRAS, 505, 5957
- Baumgardt H., Sollima A., Hilker M., 2020, PASA, 37, e046
- Beasley M. A., Leaman R., Gallart C., Larsen S. S., Battaglia G., Monelli M., Pedreiro M. H., 2019, MNRAS, 487, 1986
- Beaton R. L., et al., 2018, Space Sci. Rev., 214, 113
- Bechtol K., et al., 2015, ApJ, 807, 50
- Bechtol K., et al., 2025, arXiv e-prints, p. arXiv:2501.05739
- Bellazzini M., Gennari N., Ferraro F. R., 2005, MNRAS, 360, 185
- Belokurov V., et al., 2007, ApJ, 654, 897
- Bergemann M., Nordlander T., 2014, in Niemczura E., Smalley B., Pych W., eds., Determination of Atmospheric Parameters of B. pp 169–185, doi:10.1007/978-3-319-06956-2_16
- Bernstein R., Shectman S. A., Gunnels S. M., Mochnacki S., Athey A. E., 2003, in Iye M., Moorwood A. F. M., eds, Society of Photo-Optical Instrumentation Engineers (SPIE) Conference Series Vol. 4841, Instrument Design and Performance for Optical/Infrared Ground-based Telescopes. pp 1694–1704, doi:10.1117/12.461502
- Besla G., Kallivayalil N., Hernquist L., van der Marel R. P., Cox T. J., Kereš D., 2010, ApJ, 721, L97
- Bhardwaj A., Rejkuba M., Ngeow C.-C., Marconi M., Ripepi V., Samantaray A. S., Singh H. P., 2024, AJ, 167, 247
- Boettcher E., et al., 2013, AJ, 146, 94
- Bonnivard V., et al., 2015, MNRAS, 453, 849
- Bose S., Deason A. J., Frenk C. S., 2018, ApJ, 863, 123
- Bovy J., 2015, ApJS, 216, 29
- Bradford J. D., et al., 2011, ApJ, 743, 167
- Bressan A., Marigo P., Girardi L., Salasnich B., Dal Cero C., Rubele S., Nanni A., 2012, MNRAS, 427, 127
- Brown T. M., et al., 2014, ApJ, 796, 91
- Bruce J., Li T. S., Pace A. B., Heiger M., Song Y.-Y., Simon J. D., 2023, ApJ, 950, 167
- Bullock J. S., Boylan-Kolchin M., 2017, ARA&A, 55, 343
- Buttry R., et al., 2022, MNRAS, 514, 1706
- Cantu S. A., et al., 2021, ApJ, 916, 81
- Carballo-Bello J. Á., et al., 2016, MNRAS, 462, 501
- Carlin J. L., Sand D. J., 2018, ApJ, 865, 7
- Carlin J. L., Grillmair C. J., Muñoz R. R., Nidever D. L., Majewski S. R., 2009, ApJ, 702, L9
- Carlin J. L., et al., 2017, AJ, 154, 267
- Carlin J. L., Sheffield A. A., Cunha K., Smith V. V., 2018, ApJ, 859, L10
- Carrera R., Pancino E., Gallart C., del Pino A., 2013, MNRAS, 434, 1681
- Casey A. R., 2014, PhD thesis, Australian National University, Canberra
- Casey Q. O., et al., 2025, arXiv e-prints, p. arXiv:2501.04772
- Castelli F., Kurucz R. L., 2003, in Piskunov N., Weiss W. W., Gray D. F., eds, IAU Symposium Vol. 210, Modelling of Stellar Atmospheres. p. A20 (arXiv:astro-ph/0405087), doi:10.4550/arXiv.astro-ph/0405087
- Cerny W., et al., 2021a, ApJ, 910, 18
- Cerny W., et al., 2021b, ApJ, 920, L44
- Cerny W., et al., 2023a, ApJ, 942, 111
- Cerny W., et al., 2023b, ApJ, 953, 1
- Cerny W., et al., 2023c, ApJ, 953, L21
- Cerny W., et al., 2025, ApJ, 979, 164
- Chen Y., Girardi L., Bressan A., Marigo P., Barbieri M., Kong X., 2014, MNRAS, 444, 2525
- Chen Y., Bressan A., Girardi L., Marigo P., Kong X., Lanza A., 2015, MNRAS, 452, 1068
- Chiti A., et al., 2018a, ApJ, 856, 142
- Chiti A., Frebel A., Ji A. P., Jerjen H., Kim D., Norris J. E., 2018b, ApJ, 857, 74
- Chiti A., Frebel A., Jerjen H., Kim D., Norris J. E., 2020, ApJ, 891, 8
- Chiti A., et al., 2021, Nature Astronomy, 5, 392
- Chiti A., Simon J. D., Frebel A., Pace A. B., Ji A. P., Li T. S., 2022, ApJ, 939, 41
- Chiti A., et al., 2023, AJ, 165, 55
- Cicuñdez L., et al., 2018, A&A, 609, A53
- Circiello A., McDaniel A., Drlica-Wagner A., Karwin C., Ajello M., Di Mauro M., Sánchez-Conde M. Á., 2025, ApJ, 978, L43
- Clementini G., et al., 2023, A&A, 674, A18
- Collins M. L. M., Tollerud E. J., Sand D. J., Bonaca A., Willman B., Strader J., 2017, MNRAS, 467, 573
- Conn B. C., Jerjen H., Kim D., Schirmer M., 2018, ApJ, 852, 68
- Cooper M. C., Newman J. A., Davis M., Finkbeiner D. P., Gerke B. F., 2012, spec2d: DEEP2 DEIMOS Spectral Pipeline, Astrophysics Source Code Library, record ascl:1203.003
- Correa Magnus L., Vasiliev E., 2022, MNRAS, 511, 2610
- Correnti M., Bellazzini M., Ferraro F. R., 2009, MNRAS, 397, L26
- Crnojević D., Sand D. J., Zaritsky D., Spekkens K., Willman B., Hargis J. R., 2016, ApJ, 824, L14
- Crociati C., et al., 2023, ApJ, 951, 17
- Curtis S., Ebinger K., Fröhlich C., Hempel M., Perego A., Liebendörfer M., Thielemann F.-K., 2019, ApJ, 870, 2
- D’Onghia E., Lake G., 2008, ApJ, 686, L61
- D’Souza R., Bell E. F., 2022, MNRAS, 512, 739
- Da Costa G. S., Armandroff T. E., Norris J. E., 1992, AJ, 104, 154
- Dall’Ora M., et al., 2006, ApJ, 653, L109
- Dall’Ora M., et al., 2012, ApJ, 752, 42
- Deason A. J., Wetzel A. R., Garrison-Kimmel S., Belokurov V., 2015, MNRAS, 453, 3568
- Deras D., Cadelano M., Ferraro F. R., Lanzoni B., Pallanca C., 2023, ApJ, 942, 104
- Dooley G. A., Peter A. H. G., Carlin J. L., Frebel A., Bechtol K., Willman B., 2017, MNRAS, 472, 1060
- Dotter A., Chaboyer B., Ježremović D., Kostov V., Baron E., Ferguson J. W., 2008, ApJS, 178, 89
- Dressler A., Hare T., Bigelow B. C., Osip D. J., 2006, in McLean I. S., Iye M., eds, Society of Photo-Optical Instrumentation Engineers (SPIE) Conference Series Vol. 6269, Ground-based and Airborne Instrumentation for Astronomy. p. 62690F, doi:10.1117/12.670573
- Dressler A., et al., 2011, PASP, 123, 288
- Drlica-Wagner A., et al., 2015, ApJ, 813, 109
- Drlica-Wagner A., et al., 2016, ApJ, 833, L5
- Drlica-Wagner A., et al., 2020, ApJ, 893, 47
- Drlica-Wagner A., et al., 2021, ApJS, 256, 2
- Drlica-Wagner A., et al., 2022, ApJS, 261, 38
- Durbin M. J., et al., 2025, arXiv e-prints, p. arXiv:2505.18252
- Erkal D., Belokurov V. A., 2020, MNRAS, 495, 2554
- Erkal D., et al., 2019, MNRAS, 487, 2685
- Evans N. W., Sanders J. L., Geringer-Sameth A., 2016, Phys. Rev. D, 93, 103512
- Fanelli C., et al., 2024, A&A, 688, A154
- Fitzpatrick M., Placco V., Bolton A., Merino B., Ridgway S., Stanghellini L., 2024, arXiv e-prints, p. arXiv:2401.01982
- Flaughler B., et al., 2015, AJ, 150, 150
- Foreman-Mackey D., 2016, The Journal of Open Source Software, 1, 24
- Foreman-Mackey D., Hogg D. W., Lang D., Goodman J., 2013, PASP, 125, 306
- François P., Monaco L., Bonifacio P., Moni Bidin C., Geisler D., Sbordone L., 2016, A&A, 588, A7
- Frebel A., Norris J. E., 2015, ARA&A, 53, 631
- Frebel A., Simon J. D., Geha M., Willman B., 2010, ApJ, 708, 560
- Frebel A., Casey A. R., Jacobson H. R., Yu Q., 2013, ApJ, 769, 57
- Frebel A., Simon J. D., Kirby E. N., 2014, ApJ, 786, 74
- Frebel A., Norris J. E., Gilmore G., Wyse R. F. G., 2016, ApJ, 826, 110
- Freijli H., González-Díaz D., Geisler D., Villanova S., Muñoz C., Moni Bidin C., 2025, arXiv e-prints, p. arXiv:2502.18607
- Fritz T. K., Carrera R., Battaglia G., Taibi S., 2019, A&A, 623, A129
- Fröhlich C., Martínez-Pinedo G., Liebendörfer M., Thielemann F. K., Bravo E., Hix W. R., Langanke K., Zinner N. T., 2006, Phys. Rev. Lett., 96, 142502
- Fu S. W., et al., 2023, ApJ, 958, 167
- Gaia Collaboration et al., 2016, A&A, 595, A1
- Gaia Collaboration et al., 2018, A&A, 616, A1
- Gaia Collaboration et al., 2023, A&A, 674, A1
- Garofalo A., et al., 2013, ApJ, 767, 62
- Garofalo A., Clementini G., Cusano F., Muraveva T., Monti L., 2025, A&A, 695, A88
- Gatto M., et al., 2022, ApJ, 929, L21
- Geisler D., et al., 2023, A&A, 669, A115

- Geringer-Sameth A., Koushiappas S. M., 2011, Physical Review Letters, 107, 241303
- Geringer-Sameth A., Koushiappas S. M., Walker M. G., 2015a, Phys. Rev. D, 91, 083535
- Geringer-Sameth A., Koushiappas S. M., Walker M., 2015b, ApJ, 801, 74
- Gieles M., Erkal D., Antonini F., Balbinot E., Peñarrubia J., 2021, Nature Astronomy, 5, 957
- Gilmore G., Norris J. E., Monaco L., Yong D., Wyse R. F. G., Geisler D., 2013, ApJ, 763, 61
- Gómez F. A., Besla G., Carpintero D. D., Villalobos Á., O'Shea B. W., Bell E. F., 2015, ApJ, 802, 128
- González-Díaz D., et al., 2023, MNRAS, 526, 6274
- Greco C., et al., 2008, ApJ, 675, L73
- Hansen T. T., Smith K. M., Guhathakurta P., Dolphin A. E., Weisz D. R., Rajan A., Grillmair C. J., 2013, AJ, 146, 116
- Hankey W. J., Cole A. A., 2011, MNRAS, 411, 1536
- Hansen T. T., et al., 2017, ApJ, 838, 44
- Hansen T. T., et al., 2020, ApJ, 897, 183
- Hansen T. T., Simon J. D., Li T. S., Sharkey D., Ji A. P., Thompson I. B., Reggiani H. M., Galarza J. Y., 2024, ApJ, 968, 21
- Harris W. E., 1996, AJ, 112, 1487
- Hartley W. G., et al., 2022, MNRAS, 509, 3547
- Hayashi K., Ichikawa K., Matsumoto S., Ibe M., Ishigaki M. N., Sugai H., 2016, MNRAS, 461, 2914
- Heger A., Woosley S. E., 2010, ApJ, 724, 341
- Heiger M. E., et al., 2024, ApJ, 961, 234
- Henao L., Villanova S., Geisler D., Fernández-Trincado J. G., 2025, A&A, 696, A154
- Homma D., et al., 2018, PASJ, 70, S18
- Homma D., et al., 2019, PASJ, 71, 94
- Homma D., et al., 2024, PASJ, 76, 733
- Huang Y., et al., 2022, ApJ, 925, 164
- Hunter J. D., 2007, Computing In Science & Engineering, 9, 90
- Ishigaki M. N., Aoki W., Arimoto N., Okamoto S., 2014, A&A, 562, A146
- Ivezic Ž., et al., 2019, ApJ, 873, 111
- Jenkins S. A., Li T. S., Pace A. B., Ji A. P., Koposov S. E., Mutlu-Pakdil B., 2021, ApJ, 920, 92
- Jethwa P., Erkal D., Belokurov V., 2016, MNRAS, 461, 2212
- Jethwa P., Erkal D., Belokurov V., 2018, MNRAS, 473, 2060
- Ji A. P., Frebel A., Bromm V., 2015, MNRAS, 454, 659
- Ji A. P., Frebel A., Chiti A., Simon J. D., 2016a, Nature, 531, 610
- Ji A. P., Frebel A., Simon J. D., Geha M., 2016b, ApJ, 817, 41
- Ji A. P., Frebel A., Simon J. D., Chiti A., 2016c, ApJ, 830, 93
- Ji A. P., Frebel A., Ezzeddine R., Casey A. R., 2016d, ApJ, 832, L3
- Ji A. P., Simon J. D., Frebel A., Venn K. A., Hansen T. T., 2019, ApJ, 870, 83
- Ji A. P., et al., 2020a, AJ, 160, 181
- Ji A. P., et al., 2020b, ApJ, 889, 27
- Ji A. P., et al., 2021, ApJ, 921, 32
- Johnson C. I., Rich R. M., Caldwell N., Mateo M., Bailey John I. I., Olszewski E. W., Walker M. G., 2018, AJ, 155, 71
- Joo S.-J., et al., 2019, ApJ, 875, 120
- Jordi K., et al., 2009, AJ, 137, 4586
- Kallivayalil N., van der Marel R. P., Besla G., Anderson J., Alcock C., 2013, ApJ, 764, 161
- Kallivayalil N., et al., 2018, ApJ, 867, 19
- Karamanis M., Nabergoj D., Beutler F., Peacock J., Seljak U., 2022a, The Journal of Open Source Software, 7, 4634
- Karamanis M., Beutler F., Peacock J. A., Nabergoj D., Seljak U., 2022b, MNRAS, 516, 1644
- Karczmarek P., et al., 2015, AJ, 150, 90
- Katz H., et al., 2020, MNRAS, 494, 2200
- Keller S. C., et al., 2007, PASA, 24, 1
- Kelson D. D., 2003, PASP, 115, 688
- Kim D., Jerjen H., 2015a, ApJ, 799, 73
- Kim D., Jerjen H., 2015b, ApJ, 808, L39
- Kim D., Jerjen H., Milone A. P., Mackey D., Da Costa G. S., 2015, ApJ, 803, 63
- Kim D., Jerjen H., Mackey D., Da Costa G. S., Milone A. P., 2016a, ApJ, 820, 119
- Kim D., et al., 2016b, ApJ, 833, 16
- Kim J., Jeon M., Choi Y., Richstein H., Sacchi E., Kallivayalil N., 2023, ApJ, 959, 31
- King I., 1962, AJ, 67, 471
- Kirby E. N., Boylan-Kolchin M., Cohen J. G., Geha M., Bullock J. S., Kaplinghat M., 2013a, ApJ, 770, 16
- Kirby E. N., Cohen J. G., Guhathakurta P., Cheng L., Bullock J. S., Gallazzi A., 2013b, ApJ, 779, 102
- Kirby E. N., Simon J. D., Cohen J. G., 2015, ApJ, 810, 56
- Kirby E. N., Cohen J. G., Simon J. D., Guhathakurta P., Thygesen A. O., Duggan G. E., 2017, ApJ, 838, 83
- Kobulnicky H. A., et al., 2005, AJ, 129, 239
- Koch A., McWilliam A., Grebel E. K., Zucker D. B., Belokurov V., 2008, ApJ, 688, L13
- Koch A., Côté P., McWilliam A., 2009, A&A, 506, 729
- Koposov S. E., et al., 2011, ApJ, 736, 146
- Koposov S. E., Belokurov V., Torrealba G., Evans N. W., 2015a, ApJ, 805, 130
- Koposov S. E., et al., 2015b, ApJ, 811, 62
- Koposov S. E., et al., 2018, MNRAS, 479, 5343
- Koposov S. E., et al., 2023, MNRAS, 521, 4936
- Kuehn C., et al., 2008, ApJ, 674, L81
- Kunder A. M., Butler E., 2020, AJ, 160, 241
- Kunder A., Crab R. E., Debattista V. P., Koch-Hansen A. J., Huhmann B. M., 2021, AJ, 162, 86
- Kunder A., et al., 2024, AJ, 167, 21
- Kurtsov R., Ivanov V. D., Borissova J., Ortolani S., 2008, A&A, 489, 583
- Laevens B. P. M., et al., 2015, ApJ, 813, 44
- Larsen S. S., Romanowsky A. J., Brodie J. P., Wasserman A., 2020, Science, 370, 970
- Latour M., Kamann S., Martocchia S., Husser T. O., Saracino S., Dreizler S., 2025, A&A, 694, A248
- Leanza S., et al., 2024, A&A, 688, A133
- Lee M. G., Yuk I.-S., Park H. S., Harris J., Zaritsky D., 2009, ApJ, 703, 692
- Li T. S., et al., 2017, ApJ, 838, 8
- Li T. S., et al., 2018a, ApJ, 857, 145
- Li T. S., et al., 2018b, ApJ, 866, 22
- Limberg G., et al., 2023, ApJ, 946, 66
- Lindegren L., et al., 2021, A&A, 649, A2
- Longeard N., et al., 2018, MNRAS, 480, 2609
- Longeard N., et al., 2021, MNRAS, 503, 2754
- Loriga M., et al., 2025, A&A, 695, A156
- Lunnan R., Vogelsberger M., Frebel A., Hernquist L., Lidz A., Boylan-Kolchin M., 2012, ApJ, 746, 109
- Luque E., et al., 2018, MNRAS, 478, 2006
- Marshall J. L., et al., 2019, ApJ, 882, 177
- Martin N. F., Jin S., 2010, ApJ, 721, 1333
- Martin N. F., et al., 2016, ApJ, 830, L10
- Martin N. F., et al., 2022, Nature, 601, 45
- Martínez-Vázquez C. E., 2023, in Memorie della Società Astronomica Italiana, p. 88 ([arXiv:2409.04993](https://arxiv.org/abs/2409.04993)), doi:10.36116/MEMSAIT'94N4.2023.88
- Martínez-Vázquez C. E., et al., 2015, MNRAS, 454, 1509
- Martínez-Vázquez C. E., et al., 2019, MNRAS, 490, 2183
- Martínez-Vázquez C. E., et al., 2021a, AJ, 162, 253
- Martínez-Vázquez C. E., et al., 2021b, MNRAS, 508, 1064
- Martínez G. D., Minor Q. E., Bullock J., Kaplinghat M., Simon J. D., Geha M., 2011, ApJ, 738, 55
- Mateo M., Olszewski E. W., Walker M. G., 2008, ApJ, 675, 201
- Mau S., et al., 2019, ApJ, 875, 154
- Mau S., et al., 2020, ApJ, 890, 136
- McConnachie A. W., 2012, AJ, 144, 4
- McConnachie A. W., Côté P., 2010, ApJ, 722, L209
- McConnachie A. W., Irwin M. J., 2006, MNRAS, 365, 902
- McConnachie A. W., Venn K. A., 2020, Research Notes of the American Astronomical Society, 4, 229
- McDaniel A., Ajello M., Karwin C. M., Di Mauro M., Drlica-Wagner A., Sánchez-Conde M. A., 2024, Phys. Rev. D, 109, 063024
- McMillan P. J., 2017, MNRAS, 465, 76
- McWilliam A., Preston G. W., Sneden C., Searle L., 1995, AJ, 109, 2757
- McWilliam A., Wallerstein G., Mottini M., 2013, ApJ, 778, 149
- Medina G. E., et al., 2018, ApJ, 855, 43
- Medina G. E., Muñoz R. R., Carlin J. L., Vivas A. K., Grebel E. K., Martínez-Vázquez C. E., Hansen C. J., 2024, MNRAS, 531, 4762
- Minor Q. E., Martinez G., Bullock J., Kaplinghat M., Trainor R., 2010, ApJ, 721, 1142
- Montecinos C., Villanova S., Muñoz C., Cortés C. C., 2021, MNRAS, 503, 4336
- Morganson E., et al., 2018, PASP, 130, 074501
- Moskowitz A. G., Walker M. G., 2020, ApJ, 892, 27
- Muñoz R. R., et al., 2006, ApJ, 649, 201
- Muñoz C., et al., 2018a, A&A, 620, A96
- Muñoz R. R., Côté P., Santana F. A., Geha M., Simon J. D., Oyarzún G. A., Stetson P. B., Djorgovski S. G., 2018b, ApJ, 860, 66
- Mullen J. P., et al., 2021, ApJ, 912, 144
- Mullen J. P., et al., 2022, ApJ, 931, 131
- Musella I., et al., 2009, ApJ, 695, L83
- Mutlu-Pakdil B., et al., 2018, ApJ, 863, 25
- Mutlu-Pakdil B., et al., 2020, ApJ, 902, 106
- Nadler E. O., et al., 2020, ApJ, 893, 48
- Nadler E. O., et al., 2021, Phys. Rev. Lett., 126, 091101
- Nagasawa D. Q., et al., 2018, ApJ, 852, 99
- Navarro J. F., Frenk C. S., White S. D. M., 1996, ApJ, 462, 563

- Newman J. A., et al., 2013, ApJS, 208, 5
- Newton O., Cautun M., Jenkins A., Frenk C. S., Helly J. C., 2018, MNRAS, 479, 2853
- Nomoto K., Tominaga N., Umeda H., Kobayashi C., Maeda K., 2006, Nucl. Phys. A, 777, 424
- Nomoto K., Kobayashi C., Tominaga N., 2013, ARA&A, 51, 457
- Norris J. E., Yong D., Gilmore G., Wyse R. F. G., 2010, ApJ, 711, 350
- Oakes E. K., Hoyt T. J., Freedman W. L., Madore B. F., Tran Q. H., Cerny W., Beaton R. L., Seibert M., 2022, ApJ, 929, 116
- Oemler A., Clardy K., Kelson D., Walth G., Villanueva E., 2017, COSMOS: Carnegie Observatories System for MultiObject Spectroscopy, Astrophysics Source Code Library, record ascl:1705.001
- Ou X., et al., 2024, ApJ, 966, 33
- Pace A. B., 2024, arXiv e-prints, p. arXiv:2411.07424
- Pace A. B., Li T. S., 2019, ApJ, 875, 77
- Pace A. B., Strigari L. E., 2019, MNRAS, 482, 3480
- Pace A. B., et al., 2020, MNRAS, 495, 3022
- Pace A. B., Erkal D., Li T. S., 2022, ApJ, 940, 136
- Pallanca C., et al., 2023, ApJ, 950, 138
- Patel E., et al., 2020, ApJ, 893, 121
- Pérez F., Granger B. E., 2007, Computing in Science and Engineering, 9, 21
- Pietrzyński G., et al., 2019, Nature, 567, 200
- Placco V. M., Frebel A., Beers T. C., Stancliffe R. J., 2014, ApJ, 797, 21
- Plummer H. C., 1911, MNRAS, 71, 460
- Price-Whelan A. M., 2017, The Journal of Open Source Software, 2
- Pritzl B. J., Venn K. A., Irwin M., 2005, AJ, 130, 2140
- Richstein H., et al., 2022, ApJ, 933, 217
- Richstein H., et al., 2024, ApJ, 967, 72
- Riley A. H., et al., 2024, arXiv e-prints, p. arXiv:2410.09144
- Roederer I. U., Kirby E. N., 2014, MNRAS, 440, 2665
- Roederer I. U., et al., 2016, AJ, 151, 82
- Rosenberg A., Saviane I., Piotto G., Aparicio A., Zaggia S. R., 1998, AJ, 115, 648
- Sacchi E., et al., 2021, ApJ, 920, L19
- Salvadori S., Skúladóttir Á., Tolstoy E., 2015, MNRAS, 454, 1320
- Sand D. J., Strader J., Willman B., Zaritsky D., McLeod B., Caldwell N., Seth A., Olszewski E., 2012, ApJ, 756, 79
- Saviane I., Da Costa G. S., Held E. V., Sommariva V., Gullieuszik M., Barbuy B., Ortolani S., 2012, A&A, 540, A27
- Savino A., et al., 2022, ApJ, 938, 101
- Schlafly E. F., Finkbeiner D. P., 2011, ApJ, 737, 103
- Schlegel D. J., Finkbeiner D. P., Davis M., 1998, ApJ, 500, 525
- Sestito F., et al., 2024, A&A, 690, A333
- Shipp N., et al., 2023, ApJ, 949, 44
- Shipp N., et al., 2024, arXiv e-prints, p. arXiv:2410.09143
- Simon J. D., 2018, ApJ, 863, 89
- Simon J. D., 2019, ARA&A, 57, 375
- Simon J. D., Geha M., 2007, ApJ, 670, 313
- Simon J. D., Frebel A., McWilliam A., Kirby E. N., Thompson I. B., 2010, ApJ, 716, 446
- Simon J. D., et al., 2011, ApJ, 733, 46
- Simon J. D., et al., 2015, ApJ, 808, 95
- Simon J. D., et al., 2017, ApJ, 838, 11
- Simon J. D., et al., 2020, ApJ, 892, 137
- Simon J. D., et al., 2023, ApJ, 944, 43
- Simon J. D., et al., 2024, ApJ, 976, 256
- Simpson J. D., 2018, MNRAS, 477, 4565
- Smith S. E. T., et al., 2023, AJ, 166, 76
- Smith S. E. T., et al., 2024, ApJ, 961, 92
- Sneden C. A., 1973, PhD thesis, THE UNIVERSITY OF TEXAS AT AUSTIN.
- Sobeck J. S., Sneden C., 2023, MOOG_SCAT: Scattering version of the MOOG Line Transfer Code, Astrophysics Source Code Library, record ascl:2308.001
- Sobeck J. S., et al., 2011, AJ, 141, 175
- Souza S. O., et al., 2021, A&A, 656, A78
- Spencer M. E., Mateo M., Walker M. G., Olszewski E. W., 2017, ApJ, 836, 202
- Spencer M. E., Mateo M., Olszewski E. W., Walker M. G., McConnachie A. W., Kirby E. N., 2018, AJ, 156, 257
- Spite M., Spite F., François P., Bonifacio P., Caffau E., Salvadori S., 2018, A&A, 617, A56
- Starkenburg E., et al., 2017, MNRAS, 471, 2587
- Stetson P. B., Fiorentino G., Bono G., Bernard E. J., Monelli M., Iannicola G., Gallart C., Ferraro I., 2014, PASP, 126, 616
- Strader J., Kobulnicky H. A., 2008, AJ, 136, 2102
- Strigari L. E., Bullock J. S., Kaplinghat M., Simon J. D., Geha M., Willman B., Walker M. G., 2008, Nature, 454, 1096
- Tan C. Y., et al., 2025, ApJ, 979, 176
- Tang J., Bressan A., Rosenfield P., Slemer A., Marigo P., Girardi L., Bianchi L., 2014, MNRAS, 445, 4287
- Tau E. A., Vivas A. K., Martínez-Vázquez C. E., 2024, AJ, 167, 57
- Tody D., 1986, in Crawford D. L., ed., Society of Photo-Optical Instrumentation Engineers (SPIE) Conference Series Vol. 627, Instrumentation in astronomy VI. p. 733, doi:10.1117/12.968154
- Tody D., 1993, in Hanisch R. J., Brissenden R. J. V., Barnes J., eds, Astronomical Society of the Pacific Conference Series Vol. 52, Astronomical Data Analysis Software and Systems II. p. 173
- Tolstoy E., et al., 2023, A&A, 675, A49
- Torrealba G., Koposov S. E., Belokurov V., Irwin M., 2016a, MNRAS, 459, 2370
- Torrealba G., et al., 2016b, MNRAS, 463, 712
- Torrealba G., et al., 2018, MNRAS, 475, 5085
- Torrealba G., Belokurov V., Koposov S. E., 2019, MNRAS, 484, 2181
- Trotta R., 2008, Contemporary Physics, 49, 71
- Tsiane K., et al., 2025, arXiv e-prints, p. arXiv:2504.16203
- Vasiliev E., 2023, Galaxies, 11, 59
- Vasiliev E., 2024, MNRAS, 527, 437
- Vásquez S., et al., 2018, A&A, 619, A13
- Venn K. A., Starkenburg E., Malo L., Martin N., Laevens B. P. M., 2017, MNRAS, 466, 3741
- Virtanen P., et al., 2020, Nature Methods, 17, 261
- Vivas A. K., et al., 2016, AJ, 151, 118
- Vivas A. K., Martínez-Vázquez C., Walker A. R., 2020, ApJS, 247, 35
- Vivas A. K., Martínez-Vázquez C. E., Walker A. R., Belokurov V., Li T. S., Erkal D., 2022, ApJ, 926, 78
- Voggel K., Hilker M., Baumgardt H., Collins M. L. M., Grebel E. K., Husemann B., Richtler T., Frank M. J., 2016, MNRAS, 460, 3384
- Walker M. G., Mateo M., Olszewski E. W., Bernstein R., Wang X., Woodroofe M., 2006, AJ, 131, 2114
- Walker M. G., Mateo M., Olszewski E. W., 2009, AJ, 137, 3100
- Walker M. G., Olszewski E. W., Mateo M., 2015a, MNRAS, 448, 2717
- Walker M. G., Mateo M., Olszewski E. W., Bailey III J. I., Koposov S. E., Belokurov V., Evans N. W., 2015b, ApJ, 808, 108
- Waller F., et al., 2023, MNRAS, 519, 1349
- Walsh S. M., Willman B., Sand D., Harris J., Seth A., Zaritsky D., Jerjen H., 2008, ApJ, 688, 245
- Walt S. v. d., Colbert S. C., Varoquaux G., 2011, Computing in Science & Engineering, 13, 22
- Wan Z., et al., 2020, Nature, 583, 768
- Wang M. Y., et al., 2019, ApJ, 881, 118
- Waskom M., et al., 2016, seaborn: v0.7.0 (January 2016), doi:10.5281/zenodo.45133, <http://dx.doi.org/10.5281/zenodo.45133>
- Webber K. B., et al., 2023, ApJ, 959, 141
- Weisz D. R., et al., 2016, ApJ, 822, 32
- Wenger M., et al., 2000, A&AS, 143, 9
- Willman B., Strader J., 2012, AJ, 144, 76
- Willman B., et al., 2005, AJ, 129, 2692
- Willman B., et al., 2006, arXiv e-prints, pp astro-ph/0603486
- Willman B., Geha M., Strader J., Strigari L. E., Simon J. D., Kirby E., Ho N., Warrens A., 2011, AJ, 142, 128
- Wolf J., Martinez G. D., Bullock J. S., Kaplinghat M., Geha M., Muñoz R. R., Simon J. D., Avendaño F. F., 2010, MNRAS, 406, 1220
- Çalışkan S., Christlieb N., Grebel E. K., 2012, A&A, 537, A83
- pandas development team T., 2020, pandas-dev/pandas: Pandas, doi:10.5281/zenodo.3509134, <https://doi.org/10.5281/zenodo.3509134>
- van den Bosch F. C., Ogiya G., Hahn O., Burkert A., 2018, MNRAS, 474, 3043
- van der Marel R. P., Kallivayalil N., 2014, ApJ, 781, 121
- van der Marel R. P., Alves D. R., Hardy E., Suntzeff N. B., 2002, AJ, 124, 2639

APPENDIX

A. SEARCH FOR RR LYRAE STARS

RR Lyrae (RRL) are variable stars commonly found in old systems such as dwarf galaxies and are excellent

distance tracers (e.g., Beaton et al. 2018; Medina et al. 2024). RRL have been found in many dwarf spheroidal galaxies and Pic II with $M_V \sim -2.7$ is predicted to have $N_{\text{RRL}} \approx 1$ (Martínez-Vázquez et al. 2019; Martínez-Vázquez 2023). We utilized the *Gaia* DR3 RR Lyrae cat-

alog (Clementini et al. 2023) to search for RRL in Pic II. There are 3 RRL within 1 degree of Pic II that are consistent with the proper motion and distance modulus of Pic II, however, the closest RRL is 33.5' (or $8.8 R_h$) and all three are more distant than Pic II (distance modulus $\sim 18.4 - 18.9$ mag). Due to the large projected distance from the center of Pic II, we do not consider any of these candidate RRL to be associated with Pic II. These RRL could be associated with the LMC. In addition, the derived photometric metallicities of these three RRL ($[Fe/H] \sim -1.7$ and -1.9 dex; calculated from Mullen et al. 2021, 2022 relationships) are more consistent with the LMC or MW halo metallicity than the very metal-poor metallicity of Pic II. The absence of RRL in Pic II is not surprising as there have been reported a number of faint UFDs without RRL at similar or lower M_V (Martínez-Vázquez 2023; Tau et al. 2024).

B. LITERATURE REFERENCES FOR FIGURES

Our references are drawn from the Local Volume Database (Pace 2024)²². References for UFDs including the LMC systems (Bellazzini et al. 2005; Belokurov et al. 2007; Bhardwaj et al. 2024; Boettcher et al. 2013; Bruce et al. 2023; Cantu et al. 2021; Carlin et al. 2009, 2017; Carlin & Sand 2018; Casey et al. 2025; Cerny et al. 2021a,b, 2023a,b, 2025; Chiti et al. 2021, 2022, 2023; Cicuéndez et al. 2018; Correnti et al. 2009; Crnojević et al. 2016; Dall’Ora et al. 2006, 2012; Drlica-Wagner et al. 2015; Fritz et al. 2019; Garofalo et al. 2013, 2025; Greco et al. 2008; Hansen et al. 2024; Heiger et al. 2024; Homma et al. 2018, 2019, 2024; Jenkins et al. 2021; Ji et al. 2021; Karczmarek et al. 2015; Kim & Jerjen 2015b; Kim et al. 2016b; Kirby et al. 2013a, 2015, 2017; Koposov et al. 2011, 2015a,b, 2018; Kuehn et al. 2008; Lee et al. 2009; Li et al. 2017, 2018a; Longeard et al. 2018; Martínez-Vázquez et al. 2015; Martínez-Vázquez et al. 2019, 2021a,b; Mateo et al. 2008; McConnachie 2012; Medina et al. 2018; Moskowitz & Walker 2020; Muñoz et al. 2018b; Musella et al. 2009; Mutlu-Pakdil et al. 2018, 2020; Oakes et al. 2022; Pace et al. 2020; Richstein et al. 2022, 2024; Sand et al. 2012; Simon & Geha 2007; Simon et al. 2011, 2015, 2017; Simon 2019; Simon et al. 2020; Smith et al. 2023; Spencer et al. 2017, 2018; Stetson et al.

2014; Tan et al. 2025; Torrealba et al. 2016a,b, 2018; Vivas et al. 2016, 2020, 2022; Walker et al. 2009, 2015b,a; Walsh et al. 2008; Wang et al. 2019; Willman et al. 2006, 2011). References for ambiguous systems (Balbinot et al. 2013; Cerny et al. 2023b,c; Conn et al. 2018; Gatto et al. 2022; Homma et al. 2019; Kim & Jerjen 2015a; Kim et al. 2015, 2016a; Luque et al. 2018; Martin et al. 2016; Mau et al. 2019, 2020; Muñoz et al. 2018b; Simon et al. 2024; Smith et al. 2024; Torrealba et al. 2019). References for the GC systems (Alonso-García et al. 2025; Bandyopadhyay et al. 2025; Baumgardt & Hilker 2018; Baumgardt et al. 2020; Baumgardt & Vasiliev 2021; Bradford et al. 2011; Çalışkan et al. 2012; Carballo-Bello et al. 2016; Crociati et al. 2023; Da Costa et al. 1992; Deras et al. 2023; Fanelli et al. 2024; Frelijj et al. 2025; Geisler et al. 2023; Gieles et al. 2021; González-Díaz et al. 2023; Hamren et al. 2013; Hankey & Cole 2011; Harris 1996; Henao et al. 2025; Johnson et al. 2018; Joo et al. 2019; Jordi et al. 2009; Kirby et al. 2015; Kobulnicky et al. 2005; Koch et al. 2009; Kunder & Butler 2020; Kunder et al. 2021, 2024; Kurtev et al. 2008; Latour et al. 2025; Leanza et al. 2024; Longeard et al. 2021; Loriga et al. 2025; Montecinos et al. 2021; Muñoz et al. 2018a,b; Pallanca et al. 2023; Richstein et al. 2024; Rosenberg et al. 1998; Saviane et al. 2012; Simpson 2018; Souza et al. 2021; Strader & Kobulnicky 2008; Vásquez et al. 2018; Voggel et al. 2016; Weisz et al. 2016).

The chemical abundance references of the UFD stars in Figure 9 are as follows: Boötes I (Gilmore et al. 2013; Frebel et al. 2016; Waller et al. 2023), Boötes II (Ji et al. 2016b), Canes Venatici II (François et al. 2016), Carina II and III (Ji et al. 2020a), Cetus II (Webber et al. 2023), Grus I (Ji et al. 2019), Grus II (Hansen et al. 2020), Coma Berenices and Ursa Major II (Frebel et al. 2010), Hercules (Koch et al. 2008; François et al. 2016), Horologium I (Nagasawa et al. 2018), Leo IV (Simon et al. 2010; François et al. 2016), Pisces II (Spite et al. 2018), Reticulum II (Ji et al. 2016a,c) Segue 1 (Frebel et al. 2014), Segue 2 (Roederer & Kirby 2014), Triangulum II (Venn et al. 2017; Kirby et al. 2017; Ji et al. 2019), Tucana II (Chiti et al. 2018b, 2023), Tucana III (Hansen et al. 2017; Marshall et al. 2019), Tucana V (Hansen et al. 2024), and Ursa Major I (Waller et al. 2023).

²² Release 1.0.5 https://github.com/apace7/local_volume_database